Effects of Marsh Grass on Diffusivity

by

Jennifer Anne Sullivan

B.A. Mathematics
Boston College, 1994

Submitted to the Department of Civil and Environmental Engineering in Partial Fulfillment of the Requirements for the Degree of

Master of Science in Civil and Environmental Engineering
at the
Massachusetts Institute of Technology

June 1996

Signature of Author: .....
Department of Civil and Environmental Engineering
May 24, 1996

Certified by: .....
Heidi M. Nepf
Assistant Professor
Thesis Supervisor

Accepted by: .....
Joseph M. Sussman
Chairman, Department Committee on Graduate Studies

Effects of Marsh Grass on Diffusivity

by

Jennifer Anne Sullivan

Submitted to the Department of Civil and Environmental Engineering
on May 10, 1996 in Partial Fulfillment of the Requirements for the Degree of
Master of Science in Civil and Environmental Engineering

Abstract

The hydrodynamic processes associated with flow through vegetation have many implications for both natural and constructed wetlands. This study examined the effect of marsh grass on mixing rates. A flow visualization study was performed, using a laser light sheet and a video camera to obtain images of a plume of fluorescent dye. The study was performed in a laboratory flume, using wooden dowels to simulate plant obstructions. The effect of different densities of plants was studied, and a basic mechanical model was produced to describe the effects of the obstruction. It was found that plant/dowel density had a significant effect on mixing, an effect that is important to the function of marsh grass both as part of a wetland ecosystem and as a natural filtering system for wastewater.

Thesis Supervisor: Heidi M. Nepf

Title: Assistant Professor

Acknowledgments

This work was supported by a Lyons Fellowship.

To my parents and my sister Maureen for all their love, and for supporting me in this and all that I do.

To my advisor, Heidi Nepf, for helping me to learn so much in the past two years.

And last but not least, many thanks to all the people in the Parsons Lab who helped me out with everything from computers to experimental equipment to theoretical hydrodynamics. I couldn't have done it without the support of so many great people.

Table of Contents

List of Figures

List of Tables

1 Introduction

Wetlands play many roles in the natural environment. In recent times, as awareness of the importance of wetlands has risen, interest in the study of the many processes occurring in wetland ecosystems has also increased. One of these processes is flow through wetland vegetation. The purpose of this study is to investigate the hydrodynamic effect of vegetation on lateral and vertical mixing rates in flow through wetlands with surface-piercing vegetation.

1.1 Importance of the effects of vegetation on mixing

Wetland hydrodynamics are important to both natural and constructed wetland ecosystems. In addition to affecting the flora and fauna of the ecosystem, they also have a substantial impact on the filtering capacity of the wetland system.

1.1.1 Ecosystem effects

One way in which the hydrodynamics of flow around wetland vegetation is important is because the vegetation alters the hydrodynamic conditions in such a way as to make it more amenable to plant growth. For example, it has been suggested that the effects of vegetation on turbulence (to be described in more detail in section 1.2) aid the uptake of nutrients by the plants by creating enough turbulence to maintain the distribution of nutrients within the plant canopy despite a decrease in bed-generated turbulence and distribution due to decreased velocity (Anderson and Charters 1982, Koch 1993). Creation of turbulence also enhances nutrient uptake by thinning the laminar sublayer, thus giving the vegetation more access to nutrients by allowing more exchange between the plant bed and the free stream flow above and around it. In addition, it has been observed that the formation of wake regions around submerged vegetation is important to pollination processes (Ackerman 1986) and that the presence of vegetation causes a decrease in turbidity of surrounding water, thus providing better conditions for photosynthesis (Koch 1993).

Flow patterns through vegetation have also been shown to have an effect on fauna which inhabit vegetated areas. Eckman (1983) found that hydrodynamic effects of vegetation increased the recruitment of passive benthic organisms, probably because of decreased velocity leading to decreased erosion of small particles and microorganisms within the plant canopy. Peterson et al (1984) also found that growth in both population and size of *Mercenaria mercenaria*, a suspension-feeding bivalve, was positively

influenced by the presence of eelgrass, and attributed this fact to flow-related effects on food sources.

1.1.2 Constructed wetland implications

The hydrodynamic effect of vegetation is also important to the planning and effectiveness of constructed wetlands for wastewater treatment, a concept which has received a good deal of attention in the past few years. Understanding the magnitude of turbulence and mixing within vegetation is essential to determining how well wastes are diffused and/or absorbed within wetlands. Kadlec (1994), in his discussion of constructed wetland flow, found that the traditional methods of modeling mixing (plug flow and well-mixed models) do not apply well to wetlands, indicating that there is a need for new ways of modeling wetland mixing processes.

The ability of wetlands to retain particulate matter is another factor which is significant to the usefulness of constructed wetlands, since it leads to the removal not only of particulate contaminants, but also of dissolved contaminants which sorb on to particles (Fennessey et al 1994). The hydrodynamics of flow through vegetation play a significant role in the sedimentation and resuspension of such particulates. Increased rates of sedimentation have sometimes been found in vegetated wetland areas (Brueske and Barrett 1994, Wang et al 1993), and attributed to the reduction of flow velocity by the plant obstructions. Sedimentation processes, however, are very complicated and not very well understood, and in fact reduced sedimentation has been found within vegetation stands in some wetlands relative to nearby channels (Fennessy et al 1994). According to

the authors of that study, this is probably the result of increased resuspension caused by the larger effect of wind-induced turbulence on shallower vegetated areas than on deeper channels, and also simply of the fact that greater flow in channels means more sediment is transported there.

1.2 Previous studies of aquatic vegetation and mixing

There have been some previous studies of turbulence and mixing in flow through vegetation, but few have addressed the enhancement of mixing by plant obstructions. In fact, Leonard and Luther (1995) found a decrease in turbulence intensity in vegetated areas in a tidal marsh, and Ackerman and Okubo (1993) documented a decrease in mixing within a plant canopy. One reason why this occurs is that water velocity tends to be greatly decreased within a plant canopy, because the resistance to flow by the vegetation causes water to choose a path of less resistance around or over the canopy. For example, Gambi et al (1990) found that flow speed under a vegetative canopy was 2 to 10 times lower than in a free-stream area just upstream of the canopy. The presence of two flow zones, a much slower one within the canopy and a faster one above, was also noted by Leonard and Luther (1995). This vastly decreased velocity alone can account for a significant decrease in turbulence and mixing relative to adjacent vegetation-free zones, because bed shear, and consequently bed generated turbulence, are reduced. However, if one compares flow through vegetation to open-channel flow at the same velocity, one is likely to find that there is an increase in turbulence within the plant bed. This occurs

because vegetation presents a large number of obstructions (plants) to the flow. While the only significant turbulence in an open-channel situation is caused by either bed-generated or wind-generated shear, the additional obstructions in a vegetated area are sources of additional turbulence. Thus, while the presence of plants does decrease large-scale turbulence such as that generated by bed or wind effects (generally scaling on the depth of the water) by reducing velocity, it increases small-scale turbulence with a length scale similar to the plants' stem scale. This effect was documented by laboratory studies by Anderson and Charters (1982) and Zavistoski (1994). The effect of this smaller-scale turbulence should also show up in mixing rates.

1.3 Related areas of study

There are some related areas of study from which results could possibly be applied to wetland flow processes. One is the study of flow around cylinders, which relates in particular to this study because the plants were modeled by cylindrical dowels. Similarly, studies of cross-flow heat exchangers examine flow past confined cylindrical obstructions. Also related is the study of flow through and above crops, as applied to agriculture, and the study of the effect of trees on flow as related to the wind power industry.

1.3.1 Flow past cylinders

Most studies of flow around cylinders investigate the small-scale, instantaneous processes occurring within the wake regions of cylinders (i.e. Kourta et al 1987, Kovasznay 1948, Braza et al 1986), and many only look at flow around a single cylinder, which differs in its effects from flow through an array of cylinders (Zavistoski 1994). This can especially be noticed in an overview of flow visualization studies compiled by Coutanceau and Defaye (1991), where the images obtained are mostly of single-dowel, near-dowel effects. In addition, since many such experiments were performed in wind tunnels, the Reynolds numbers for those experiments are significantly higher than those typically encountered in water flow (i.e. Kourta et al 1987, Higuchi et al 1989).

Cylinder flow studies are useful, however, in that they document somewhat the wakes caused by dowel-type obstructions. These turbulent wakes, the product the periodic shedding of Karman vortices, are a well-known phenomenon, and have been documented in several papers on the subject of flow around cylinders (i.e. Braza et al 1985, Kourta et al 1986, Coutanceau and Defaye 1991). Kovasznay (1948), found that the critical Reynolds number for the formation of vortices was 40, which indicates that the flow velocities studied here are within an appropriate range for a well-formed vortex wake.

1.3.2 Cross-flow heat exchangers

Studies of cross-flow heat exchangers also tend to focus on near-dowel effects, in order to determine their effect on heat diffusion between the dowel and the surrounding fluid (Zukauskas and Ziugzda 1985). Otherwise, they also are concerned with the effects of turbulent buffeting on the cylinders (Walker, 1982), an effect which may have significance with regard to plant morphology because of the effects of external stresses on the manner in which plant stems and leaves prefer to grow, but which does not relate to this particular study. In addition, because the cylinders in cross-flow heat exchangers are placed in rows (Kundu et al 1991), the interaction between cylinders is completely different from that in a randomly placed array such as would be found in wetland vegetation.

1.3.3 Flow through crops and trees

Studies of the effects of crops (i.e. Plate and Quraishi 1965, Seginer et al 1976, Raupach and Thom 1981, Jacobs et al. 1995) and of trees (i.e. Meroney 1968, Nierenberg 1993, Elliott and Barnard 1990) tend to look at vegetation as roughness elements and to concentrate on flow at the top of and above the canopy. Several of these studies look at within-canopy effects, but not in the same manner as they are studied here. Plate and Quraishi (1965) and Raupach and Thom (1981) considered the entire plant canopy as being part of the boundary layer. Jacobs et al (1995) looked at the effects of temperature

differences within crop canopies on advection. In addition, within-canopy flow in an unconfined canopy differs from that in a confined canopy. In unconfined plant canopies, turbulence is largely generated by shear between the faster flow above the canopy and the slower flow within the canopy (Seginer et al 1976), so plant-induced turbulence effects are less significant to such configurations than to confined flows.

1.4 Structure of this thesis

The laboratory experiment performed for this research is described in Chapter 2. Results of the experiment are briefly described in Chapter 3, and Chapter 4 presents a mechanical model for diffusion within a plant array and correlates the results of the model with the experimental results. Chapter 5 discusses the outcome of the project and proposes areas for further study.

2 Experimental Procedure

2.1 Equipment

2.1.1 Flume and Current

These experiments were conducted in a 38 cm wide, 24 m long flume in the Parsons Laboratory at MIT (Figure 1. NOTE: None of the drawings presented in this thesis are to scale). The flume was filled to a depth of 15 cm. Recirculating current produced by a pump running under a flume was varied between 27 and 110 gallons per minute.

2.1.2 Turbulence Damping

Because a significant amount of large-scale turbulence was evident at the inlet, several methods were used to minimize the effect of this turbulence. At the inlet, 2 pieces

of 6 cm thick rubberized coconut fiber were placed between the outlet tube and the bottom of the flume to cut out large-scale turbulence in the entering water (See Figure 1).

A 122 cm long array of dowels (approximately 5.5% dowels by base area) in a Plexiglas bottom was placed 145 cm from the inlet to further damp large-scale turbulence. There was some concern that the small-scale turbulence created by this preliminary array would affect flow patterns in the test section. However, based on the measurements of Zavistoski (1994), the disturbance seen in velocity and turbulence intensity measurements behind a dowel of this size disappears within 33 dowel diameters. Since the test section of the flume was over 600 diameters from the initial dowel array, it was clear that it was far beyond the region of influence of small-scale turbulence. Likewise, Kovasznay (1948) made measurements showing that the velocity disturbance resulting from a cylinder disappeared within 100 dowel diameters, also a much shorter distance than that between the initial array and the test section.

As a final measure, 2 flow straighteners were placed in series, 124 cm apart, just upstream of the test section. The flow straighteners were 46 cm long, 15 cm tall, and 38 cm wide, and consisted of 1.9 cm tubes running in the direction of the flow. Placement of the flow straighteners and other turbulence-damping apparatus was determined visually by using a dye stream to track turbulence in the flow.

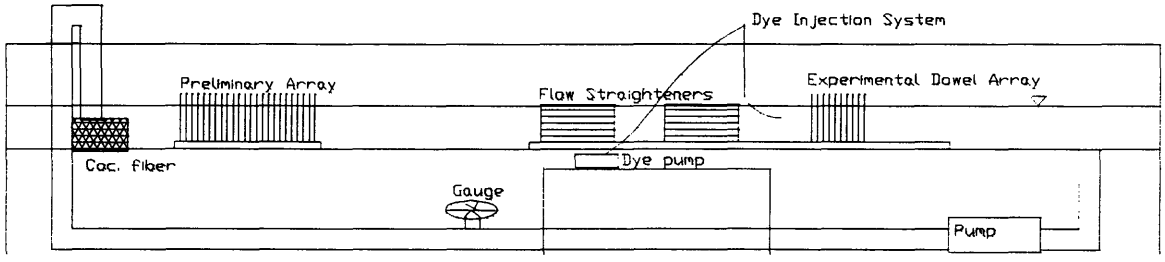

Figure 1: Flume Setup

2.1.3 Simulated Plants

Vegetation was simulated using 0.6 cm diameter, 20 cm long dowels standing upright in holes drilled in a Plexiglas false bottom. 38 cm wide, 120 cm long and 1.26 cm thick. These model plants were originally devised by Zavistoski (1994) based on dimensions of cordgrass (*Spartina alterniflora*) stalks. Because of the inflexibility of the model plants, they most accurately model the stems of *Spartina* and other grasses, as well as woody plants such as shrubs and trees. They do not accurately represent the flexible leafy areas of grasses and other plants.

Three different densities of dowel array were used in addition to the null case. The highest density was 5.3% dowels by area (1900 dowels/m^2), the medium density was 1.4% (480 dowels/m^2) and the lowest density was 0.6% (230 dowels/m^2). These densities were chosen to represent three different levels of near-wake interaction - no interaction for the low density case, high interaction for the high density case, and an intermediate range for the medium density (for a more detailed description, see Zavistoski 1994). For the highest density, all the holes in the Plexiglas were filled with dowels. For the medium, low and null cases, only an appropriate number of holes had dowels inserted in them, and the remaining holes were plugged with black RTV silicone rubber to limit any roughness effects due to the holes.

To reduce the effects of bottom discontinuity, two sheets of plain Plexiglas were placed upstream of the sheet with the dowel array in it. The three Plexiglas sheets were held together by 5 cm long, 0.6 cm diameter stainless steel rods inserted in holes in the

ends of the sheets. This provided for proper alignment of the sections, which ensured that the bottom was smooth throughout. The flow straighteners described above were placed on the Plexiglas bottom, to further reduce any edge effects.

2.1.4 Dye Pumping System

Fluorescein dye was used at a very high concentration so that it would be visible even as it became somewhat mixed. The dye was pumped in to the flume at approximately mid-depth and mid-width, 54 cm upstream of the beginning of the dowel. The central position with respect to depth and width was chosen to keep the dye from interacting too much with the edges of the flume. The distance from the injection point to the dowel array was chosen because it allowed approximately 1 meter for the dye to advect and diffuse before reaching the measurement point. This allowed some time for the dye to diffuse, making the plume wide enough to get a good comparison between different trials.

The dye injecting system used two types of tubing. A length of Tygon tubing with an inner diameter of 1/8" and an outer diameter of 1/4" ran from the pump to a piece of stainless steel tubing with outer diameter 1/8" and inner diameter 1/16". Very small tubing was used so as to minimize the effect of the tubing on turbulence patterns. The stainless steel tubing was inserted in a hole in a small board placed across the top of the flume, and had a 90° bend at the appropriate depth, so that the dye was flowing in the same direction as the water flow at the point of injection (Figure 2).

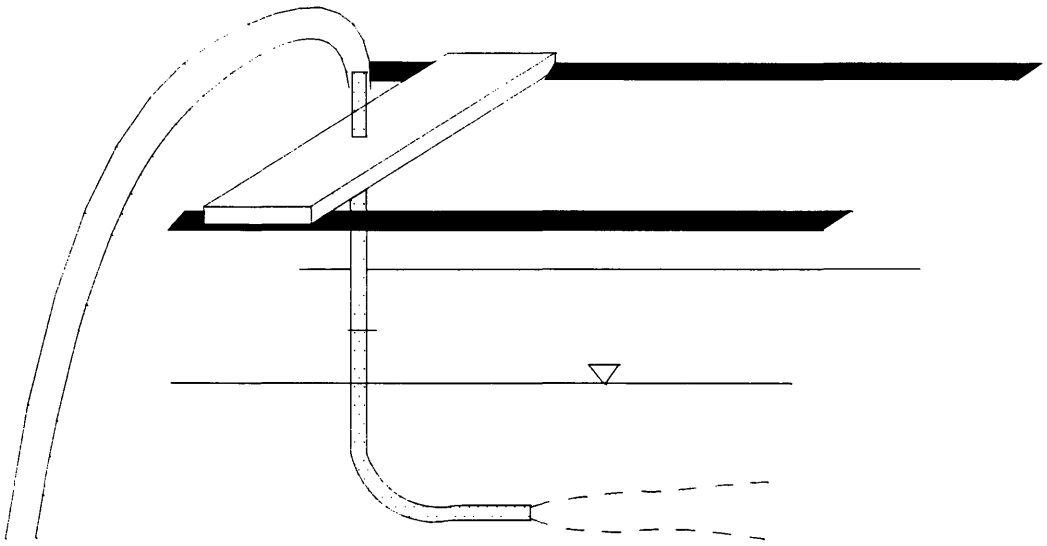

Figure 2: Dye injection system

The dye was injected at a velocity close to that of the water flow, in order to eliminate as much as possible any mixing due to shear associated with the velocity of the injected dye. For this reason, two different pumps were used, one for the higher velocities and one for the lower velocities. For the two lowest velocities, a Harvard Apparatus syringe pump was used, because syringe pumps can produce low flows in a very precise and steady manner. Since the two higher velocities called for flow rates beyond the capabilities of the syringe pump, a Cole Parmer Masterflex peristaltic pump was used for these cases.

In order to achieve the appropriate speed for the entering dye, corresponding flow rates were calculated using the desired velocities and the cross-sectional area of the

tubing. With the syringe pump, it was possible to enter this flow rate directly into the pump. With the peristaltic pump, the pump control was too inaccurate at these flow rates to be used directly. Therefore for those cases the velocity in the clear Tygon tubing was measured visually using a stopwatch, and the pump adjusted until the appropriate velocity was reached.

2.1.5 Laser Setup

The dye plume was illuminated using a 300 mW blue-green argon-ion laser from Ion Laser Technology. The laser was placed such that its beam ran parallel to the flume (Figure 3). First the beam was run through a 5X microscope objective lens to expand the beam. This was done so that the resulting lightsheet would be thick enough (approximately 1 cm) to provide some depth-averaging of the dye plume, thus smoothing the visible dye distribution and reducing the amount of time over which the resulting images had to be averaged.

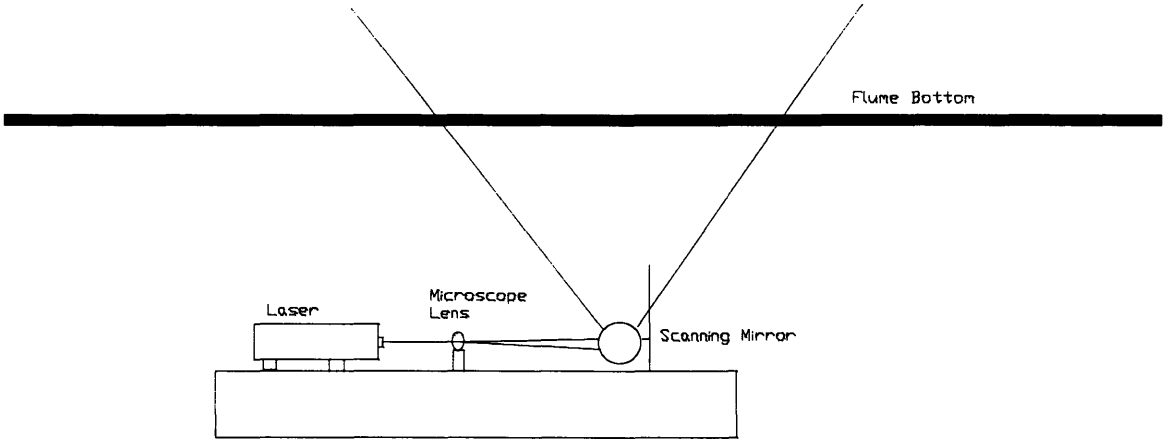

Figure 3a: Vertical Setup (side view)

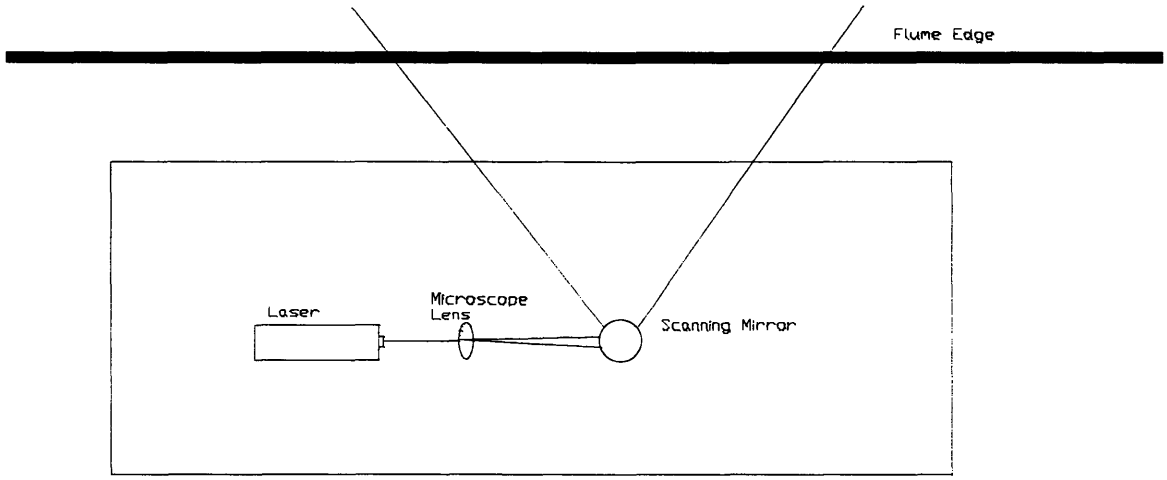

Figure 3b: Horizontal Setup (top view)

Figure 3: Laser Setup

Initially, the beam was expanded using two lenses, the microscope lens to expand it and an achromatic lens to straighten the beam so it would stay at a steady thickness throughout the flume. This setup was extremely difficult to align, and the effect of the expansion of the beam from one edge of the flume to the other without the achromatic lens was determined not to be significant, even though the actual expansion in thickness was 10-20% of the entering thickness. It could be expected that the expansion of the beam would have little effect, since any brightening effect of the expansion of width of the beam would be counteracted by the decreased light intensity of the wider beam. Thus, the only real effect of the beam expansion would be increased depth-averaging from one edge of the flume to another, which would not have a significant effect on the results since the images studied were time-averaged over many frames anyway. It was actually found that the pixel intensity resulting from the ambient light decreased from the near to the far edge of the flume, a phenomenon which can be attributed to the absorption of light by the dye cloud.

The expanded laser beam was then deflected by a Lincoln Laser Company scanning mirror to create a lightsheet shining into the flume. A scanning mirror was used because it produces a light sheet of uniform intensity, unlike a cylindrical lens which creates a sheet of uneven intensity (see Figure 4). For the trials in which lateral mixing was examined, the laser was placed beside the flume so that the lightsheet shone into the flume from the side at a height of approximately 7 cm from the bottom (the height at which the dye was injected). For the analysis of vertical mixing, the laser was placed on a platform below the flume, and the light sheet shone up through the flume at the centerline (Figure 3).

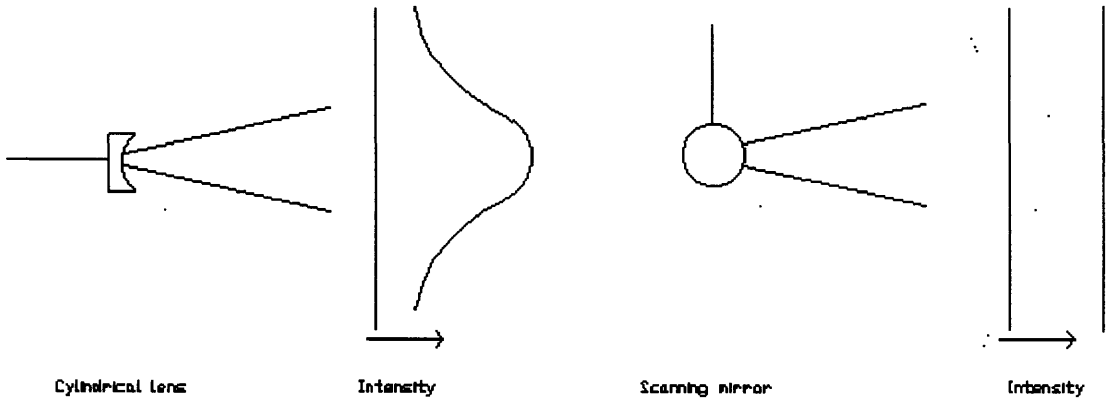

Figure 4: Difference between cylindrical lens and scanning mirror

2.1.6 Video Camera

The video footage of the dye was taken using a Minolta CR1200 camera. The camera was chosen because it had a manual iris control. A camera with an automatic iris control makes automatic adjustments to different light conditions, making it difficult to monitor the extent to which the camera picks up both the illuminated dye stream and other light sources. The camera was mounted on a Slik Universal U212 Deluxe tripod. For the vertical visualization, the tripod was placed beside the flume and the camera mounted in the standard manner. For the lateral case, the tripod was adjusted so that the camera could be suspended above the flume, facing directly down into the flume (Figure 5).

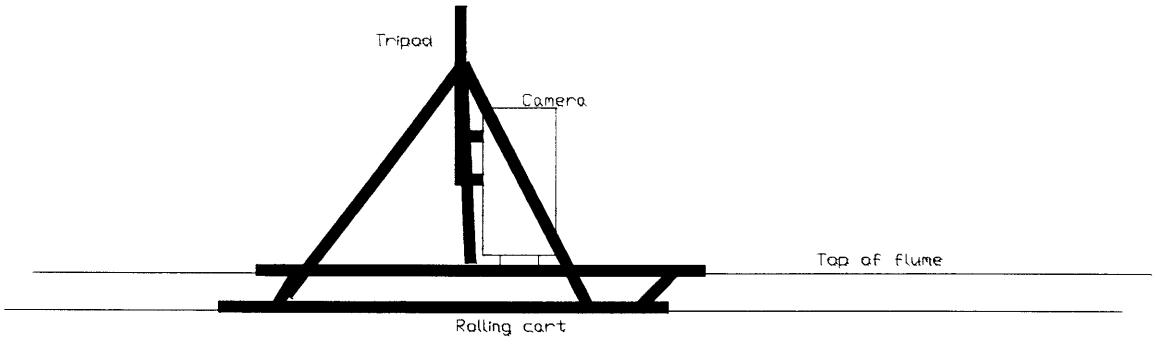

Figure 5a: Lateral Setup

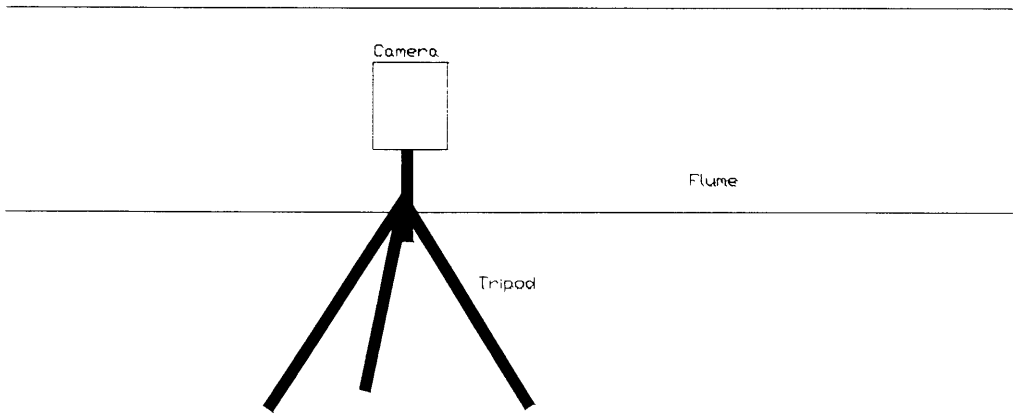

Figure 5b: Vertical Setup

Figure 5: Camera Setup

2.2 Velocity Measurement

Four flow velocities were used in the experiment. The velocities used were 3 cm/s, 6 cm/s, 9 cm/s and 12 cm/s (±0.3 cm/s), as measured downstream of the test area in an undisturbed portion of the flume. Velocities were measured using a Sontek Acoustic Doppler Velocimeter, with the average velocity taken over 100 seconds.

The measured velocities needed to be adjusted before being used for calculations, to account for the effects of the false bottom and the dowels on cross-sectional area. This was done using the mass balance equation, assuming that surface elevation was constant throughout the flume. Using the basic equation

$$A_m u_m = A_t u_t \tag{2.2.1}$$

where A_m=cross-sectional area at velocity measurement point, u_m= measured velocity, A_t=cross-sectional area of test section and u_t=velocity in test section, one gets that

$$u_t = \frac{A_m}{A_t} u_m \tag{2.2.2}$$

For this case,

$$\frac{A_m}{A_t} = \frac{h_m}{h_t} = \frac{16.3cm}{15cm} = 1.09 \tag{2.2.3}$$

so the actual velocity within the test section is 1.09 times the measured velocity just downstream. A similar analysis was performed for the dowel obstructions, using the average fraction of the flow cross-section taken up by dowels. It was found that only the medium and high densities had a significant effect, so the velocities for those two cases were appropriately adjusted. Actual velocities after adjustment are shown in Table 1.

Table 1: Adjusted velocities

Lateral					
Free-stream	Null	Low	Medium	High	Average
3	3.4	3.2	3.1	3.5	3.3
6	6.3	6.3	6.4	6.4	6.4
9	9.9	9.9	10.1	9.9	10
12	13.3	13.3	13.2	13.4	13.3

Vertical					
Free-stream	Null	Low	Medium	High	Average
3	3.1	3.2	3.3	3.5	3.3
6	6.4	6.9	6.7	6.4	6.6
9	9.7	9.8	9.7	10.2	9.9
12	12.9	13	13.2	13.3	13.1

The Reynolds numbers associated with these velocities was computed in two ways, using both the depth of the water and the dowel diameter as length scales. The depth-scale Reynolds number, Re_h, was

$$\mathrm{Re}_h = \frac{uh}{\nu} \tag{2.2.4}$$

where u = average velocity, h = water height, and ν = the kinematic viscosity of water. For these cases, the Reynolds numbers ranged from 4,650 to 20,100 (see Table 2) . The dowel-diameter-based Reynolds number, Re_d, is, however, probably a more appropriate scale to use in this case, due to the large impact of the vegetation in this kind of situation (Kadlec 1990). This number, defined as

$$\mathrm{Re}_d = \frac{ud}{\nu} \tag{2.2.5}$$

where d = dowel diameter, ranged from 192-804. This range of Reynolds numbers is well above the critical Reynolds number for vortex formation of 40 found by Kovasznay (1948), so all of these cases were well within his vortex-shedding regime. However, it must be noted that Zavistoski (1994) found R_{crit} in a setup like this one to be between 360 and 380, which would mean that this range of Reynolds numbers includes flow in both regimes.

2.3 Video Footage

For each velocity/dowel density combination, 2 minutes of video footage were taken for later analysis. The video camera was placed such that the image spanned the width of the flume for the lateral images, and the water height for the vertical case. The placement was such that profiles of the illuminated dye could be taken approximately 1 meter downstream of the dye injection point (actual distances ranged from 76.1 to 91.7 cm, varying from one case to another), in the middle of the dowel array.

Table 2: Range of Reynolds numbers

Lateral diffusion:					
Free-stream velocity	Depth Re:				
	Null	Low	Medium	High	Average
3	5100	4800	4650	5250	4950
6	9450	9450	9600	9600	9530
9	14850	14850	15150	14850	14900
12	19950	19950	19800	20100	20000
	Diameter Re:				
	Null	Low	Medium	High	Average
3	204	192	186	210	147
6	378	378	384	384	381
9	594	594	606	594	597
12	798	798	792	804	798

Vertical diffusion:					
Free-stream velocity	Depth Re:				
	Null	Low	Medium	High	Average
3	4650	4800	4950	5250	4910
6	9600	10350	10050	9600	9900
9	14550	14700	14550	15300	14800
12	19350	19500	19800	19950	19700
	Diameter Re:				
	Null	Low	Medium	High	Average
3	186	192	198	210	197
6	384	414	402	384	396
9	582	588	582	612	591
12	780	792	798	798	792

2.4 Changes in Procedure

The initial video footage was taken with all the dowels in place, but for the lateral low and medium density cases, as well as all the high density cases, the image was affected by blockage of the laser light by the dowels, so those cases were redone with all dowels beyond the desired measurement area removed. This provided for a much clearer image, but did not affect the results because the configuration up to the measurement point was the same (Figure 6).

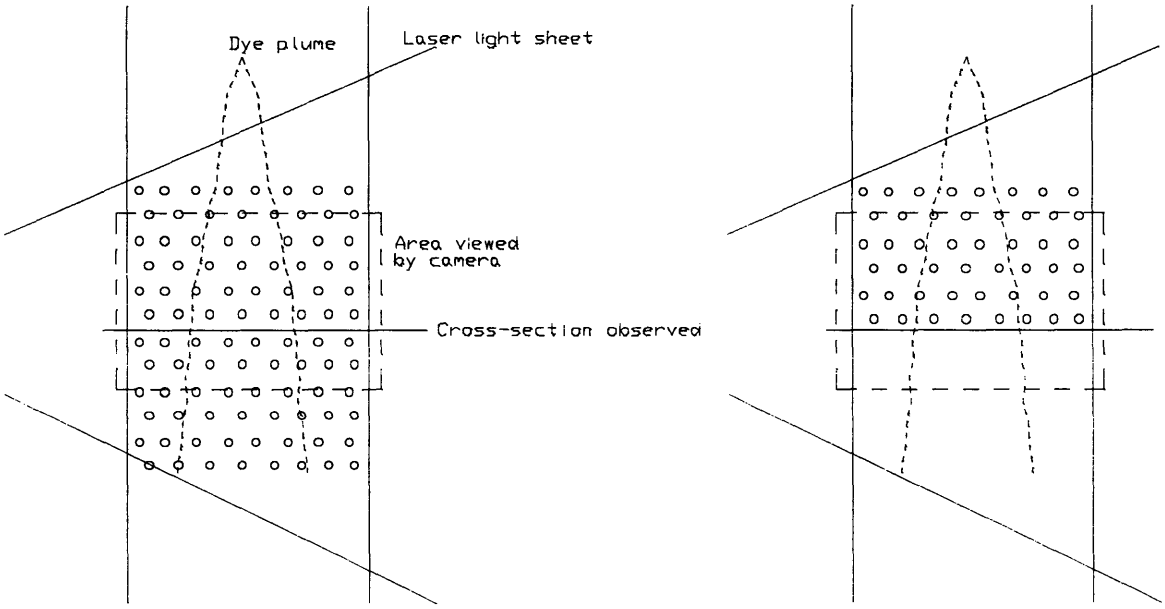

Figure 6: Original and modified dowel arrangements

Another major problem encountered was the effect of illumination of the dowels and the flume by both ambient light and the laser light. Several measures had to be taken to ensure a dark enough background to make the dye stream fully visible. Black posterboard was taped to the sides and bottom of the flume in the test area, with only a small slit exposed to the outside for the laser light sheet to enter through. Black felt was also draped over the top of the flume and the tripod and camera setup. In addition, both the dowels and the Plexiglas in the array were spray-painted black, and nearly all the lights in the room were turned out to ensure total darkness.

2.5 Data analysis

2.5.1 Advection-Diffusion Theory

The mixing coefficients for the different cases explored here were found by comparing the pixel intensity data to the Gaussian curves defined by advection-diffusion theory. This was accomplished using the three-dimensional advection-diffusion equation. For a continuous release, the concentration distribution is

$$C(x,y,z) = \frac{\dot{M}}{4\pi x\sqrt{D_y D_z}} e^{\left(\frac{-y^2 u}{4D_y x} \frac{z^2 u}{4D_z x}\right)}, \qquad (2.5.1)$$

where x is longitudinal (streamwise) distance from the dye outlet, y is lateral distance, z is vertical distance, $\dot{M}$ is the amount of dye entering in mass per unit time, and D_y and D_x are the lateral and vertical mixing coefficients.

First it must be noted that this equation does not account for diffusion or dispersion in the longitudinal direction. This assumption can be made because the Peclet number for longitudinal dispersion, based on the velocity and distance data from these experiments and the value for longitudinal dispersion found by Mugnier (1995), is

$$Pe = \frac{ul}{D_z} = \frac{(3.1\,cm/s)(76.1\,cm)}{6\,cm^2/s} = 38.05 >> 1 \qquad (2.5.2)$$

Thus, longitudinal dispersion can be safely ignored.

Equation 2.5.1 was further simplified in order to study diffusion in only the y or z direction. For example, if z is taken to be zero, which it is in the lateral case here because the laser is at the vertical center of the dye cloud, the equation becomes

$$C(x,y,z) = \frac{\dot{M}}{4\pi x\sqrt{D_y D_z}} e^{\frac{-y^2 u}{4D_y x}} \qquad (2.5.3)$$

The maximum concentration, at the lateral center of the cloud, is then

$$C_{max} = \frac{\dot{M}}{4\pi x\sqrt{D_y D_z}} \qquad (2.5.4)$$

and the equation for normalized dye distribution can be found by dividing by this C_{max}:

$$C_{norm}(x,y) = e^{\frac{-y^2 u}{4D_y x}} \qquad (2.5.5)$$

Using the fact that $t=x/u$, this becomes:

$$C_{norm}(y,t) = e^{\frac{-y^2}{4D_y t}} \qquad (2.5.6)$$

the equation which was used to determine D_y. A similar process can be used to show that the same equation applies for D_z, with z^2 replacing y^2 and D_z replacing D_y.

2.5.2 Image Processing

Final images were scanned in to a computer using Global Lab Image® software. For each case, an average of 100 frames was created using a routine available in the software (Figure 8). In addition, 1 to 5 instantaneous images (Figure 9) were saved for comparison between average and instantaneous photographs. All figures in the section are from the low-density, 6 cm/s lateral case.

The first step in analyzing the data was to use the Global Lab Image software to take a pixel intensity profile laterally spanning the dye plume for each image (Figure 7). These profiles were then smoothed and normalized using Matlab (see Appendix 1 for the Matlab program used to do this), to produce a profile representative of the dye distribution.

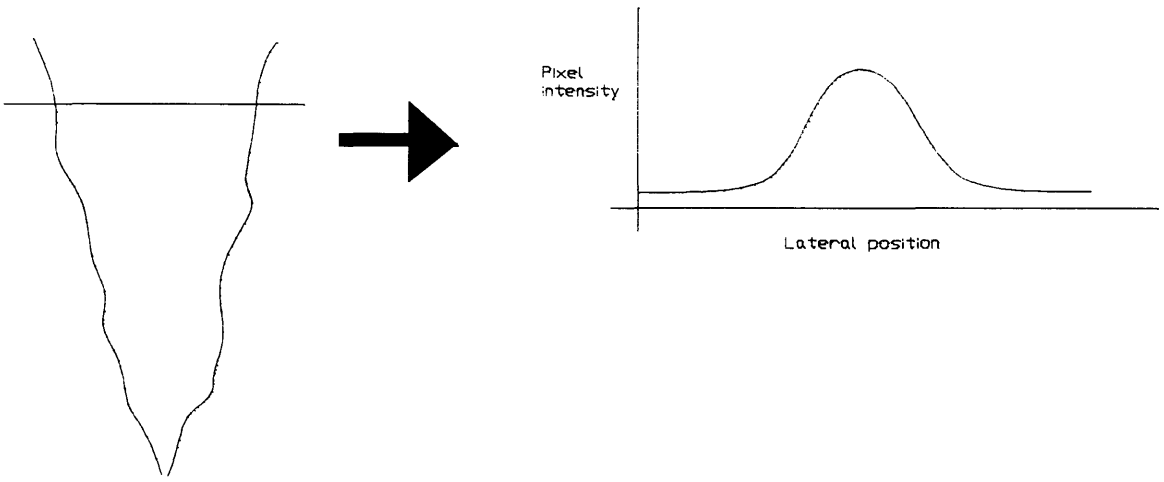

Figure 7: Conversion of data

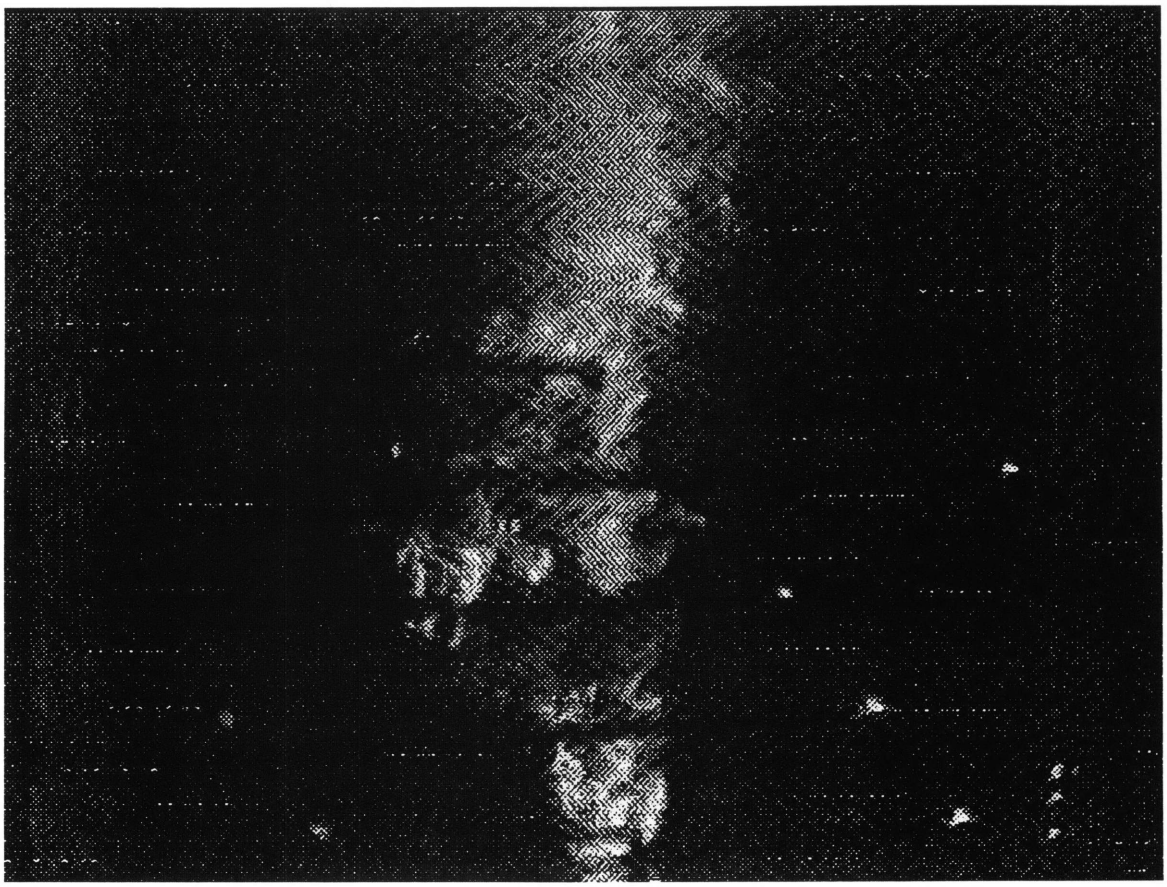

|----------38 cm----------|

Figure 8: Instantaneous image

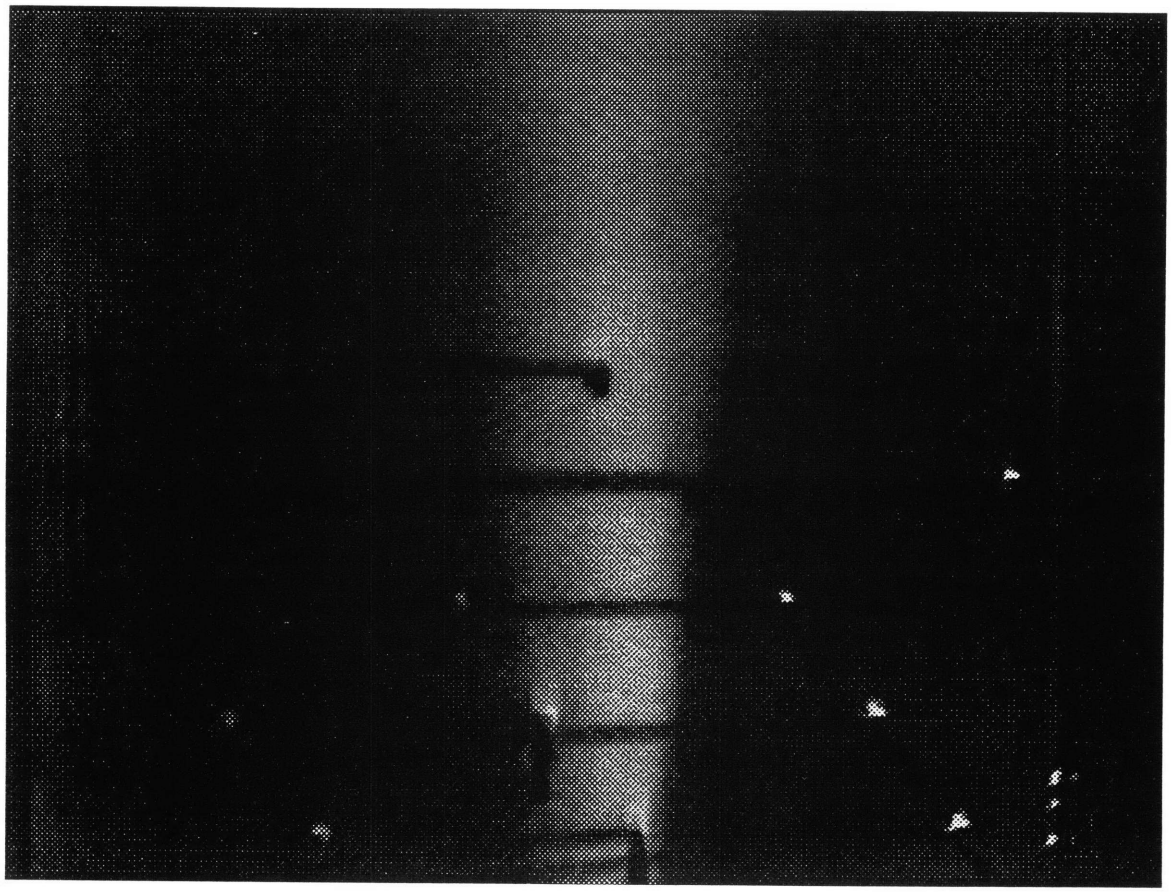

|----------38 cm----------|

Figure 9: Averaged image

2.5.3 Analysis of Dye Profiles for Diffusion Coefficient

Because there is a linear relationship between pixel intensity (brightness) and dye concentration, it was possible to use the profiles of pixel intensity to find D, the coefficient of diffusion. This was done by using the Microsoft Excel Solver to find the theoretical Gaussian curve which best matched the data curve for each case (Figure 10). Although the pixel intensity from the data appears to drop below zero after a certain point, this is actually just an artifact of the way the data was normalized and of the fact that brightness decreased somewhat upon passing through the dye plume.

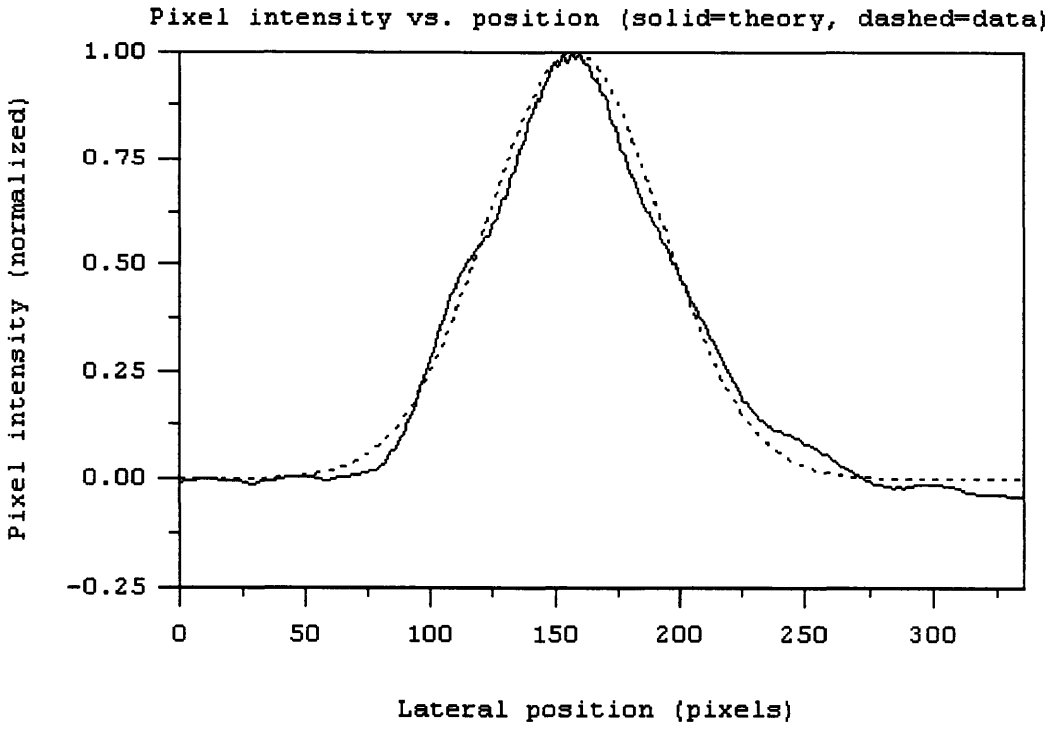

Figure 10: Match of Gaussian curve to data

For the null cases, Equation 2.3.5 was used to construct the theoretical curve. Due to uncertainty in the placement of the dye injection system, the centerline of the dye plume could not be determined accurately, so the edge of the flume was used as a reference point instead. Thus the value (y-c) was used instead of y, with c the position of the center of the plume (the point where C=C_{max}) relative to the wall.

For the cases involving dowels, the equation had to be reformulated to account for the fact that the dye traveled some distance in the dowel-free zone upstream of the dowel array before entering the array. The basic equation was adapted to find the diffusion coefficient within the array by solving the equation for diffusion starting from an initial spatial distribution

$$C(y,t) = \int_{-\infty}^{\infty} \frac{f(y_i)}{4\pi D_y t} e^{\frac{(y-y_i)^2}{4D_y t}} dy_i \qquad (2.5.7)$$

where $f(y_i)$ is the initial spatial distribution of the dye (Fischer et al 1979). For this analysis, the initial spatial distribution used was the Gaussian distribution of the dye upon entering the dowel array. The resulting equation for the distribution exiting the array (normalized) is

$$C_{norm}(y,t) = e^{\frac{-(y-c)^2}{4(D_i t_i + Dt)}} \qquad (2.5.8)$$

where D_i and t_i are the diffusion coefficient for, and time spent within, the region preceding the dowel array, and D and t are the parameters within the dowel array. D_i was taken from the measurement for the null case. The two time periods, t_i and t, were based

on the length of each section and the weighted velocities based on the dowel velocity effect. D and c were again optimized to determine D within the dowel array.

It was also noted for some of the vertical cases that, due to the effects of gravity and diffusion, the dye cloud intersected the bottom of the flume as it evolved downstream. For these cases, the effect of the bottom was treated as a reflection of the curve, so that the resulting distribution would be that of two Gaussian curves, one (the initial distribution) centered at the usual center, and the other (the reflected dye) centered outside the flume in a mirror image of the inital distribution (Figure 11).

The total dye concentration (or pixel intensity) at any point would therefore be the sum of the values of two curves:

$$C_{norm}(z,t) = e^{\frac{-(z-c)^2}{4(D_i t_i + Dt)}} + e^{\frac{-(2z_{max}-z-c)^2}{4(D_i t_i + Dt)}} \qquad (2.5.9)$$

where the first term is the initial distribution curve and the second term accounts for the reflection (Fischer et al 1979).

For all cases, the time t was calculated from the velocity, and c (position of the centerline) and D were optimized. The fit of the theoretical Gaussian curve to the data curve was determined by taking the root mean square of the differences between the two at each point along the curve

$$E = \sqrt{\sum_i (C_{theoretical} - C_{data})_i^2} \qquad (2.5.10)$$

where C is normalized concentration/pixel intensity. This value was minimized to determine the value of D for the best matching curve (See Figure 12 for an example of how E varies with D, again using the 6 cm/s low density case).

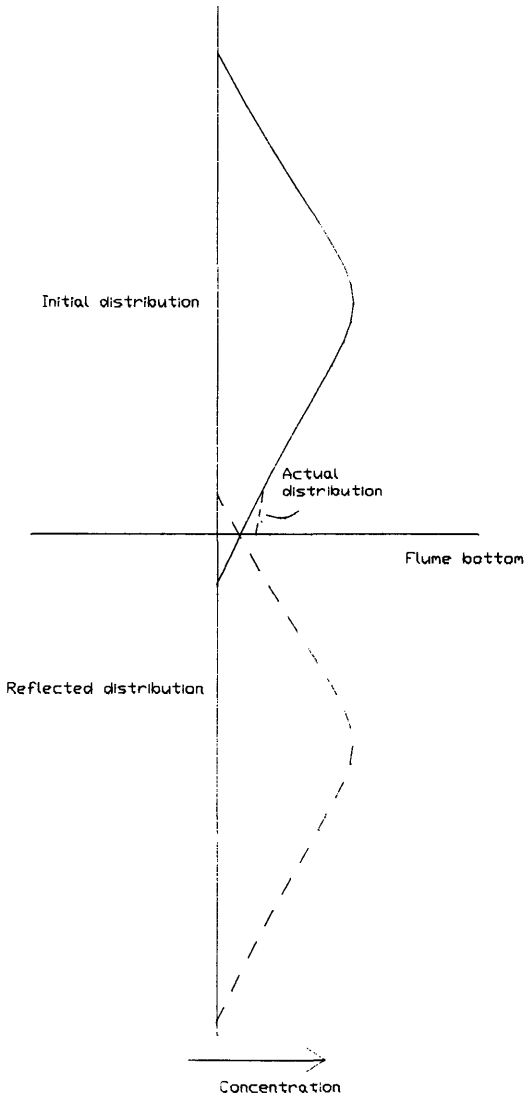

Figure 11: Reflected dye distribution

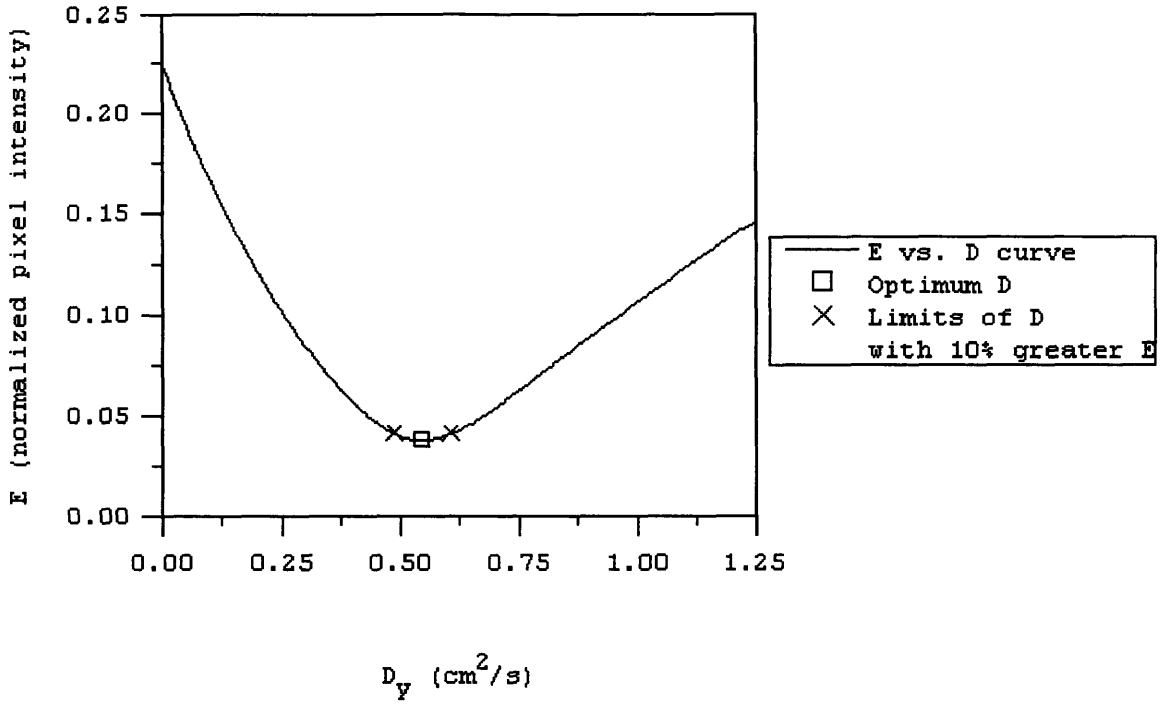

Figure 12: Variation of error with D_y

2.5.4 Uncertainty Analysis

There were two main potential sources of error in the determination of the diffusion coefficient. One was experimental error and the other was analysis error in the match of the data curve to a Gaussian curve. Possible sources of experimental error were placement of the laser (i.e. variations in thickness and depth of the lightsheet), levels of ambient light, placement of the dye injection apparatus and placement of the camera.

Attempts were made to eliminate the effects of experimental error as much as possible. In order to account for shifts in camera position, the distance of the camera from the injection point was recalibrated several times throughout the experiments. Lateral/vertical shift in dye injection point was accounted for by redetermining the center of the dye plume for each case. Normalization of the pixel intensity data should have eliminated most effects of changes in lightsheet thickness and ambient light.

Error bars were determined, therefore, from the process of fitting the theoretical curves to the data. While D was chosen as the D for which the rms error between the data curve and the theoretical curve was minimized, there were obviously other values of D which constituted possible matches. The values of D for a 10% increase in rms difference between data and theory were used to determine a value of the uncertainty for each value of D. See Figure 12 for the placement of these values on the D vs. E curve. The uncertainty was taken to be one-half the difference between the upper and lower limits of the range of potential solutions with error within 10% of the original error. This quantified error by indicating how many values of D were potential fits to the data.

2.5.5 Analysis of Dye Profiles for C_{rms}

For each lateral case, the averaged and instantaneous profiles were also compared in an attempt to quantify the effect of the dowel array on small-scale mixing. This was done by evaluating the root mean square fluctuation of concentration, defined as

$$C_{rms} = \sqrt{\frac{\sum (C_{inst.} - C_{avg.})^2}{N}} \qquad (2.5.11)$$

to compare the pixel intensities at each of the N points on each instantaneous and corresponding averaged profile (See Figure 13 for an illustration of the contrast between an average profile and an instantaneous profile). To reduce the effects of meandering (which can be seen in the example) on the instantaneous profile, the data points from 5 instantaneous images were amalgamated and examined. The uncertainty of these averages was determined by finding values using only four of the five profiles and using the root mean square of the differences between those values and the five-profile value as an indicator of uncertainty.

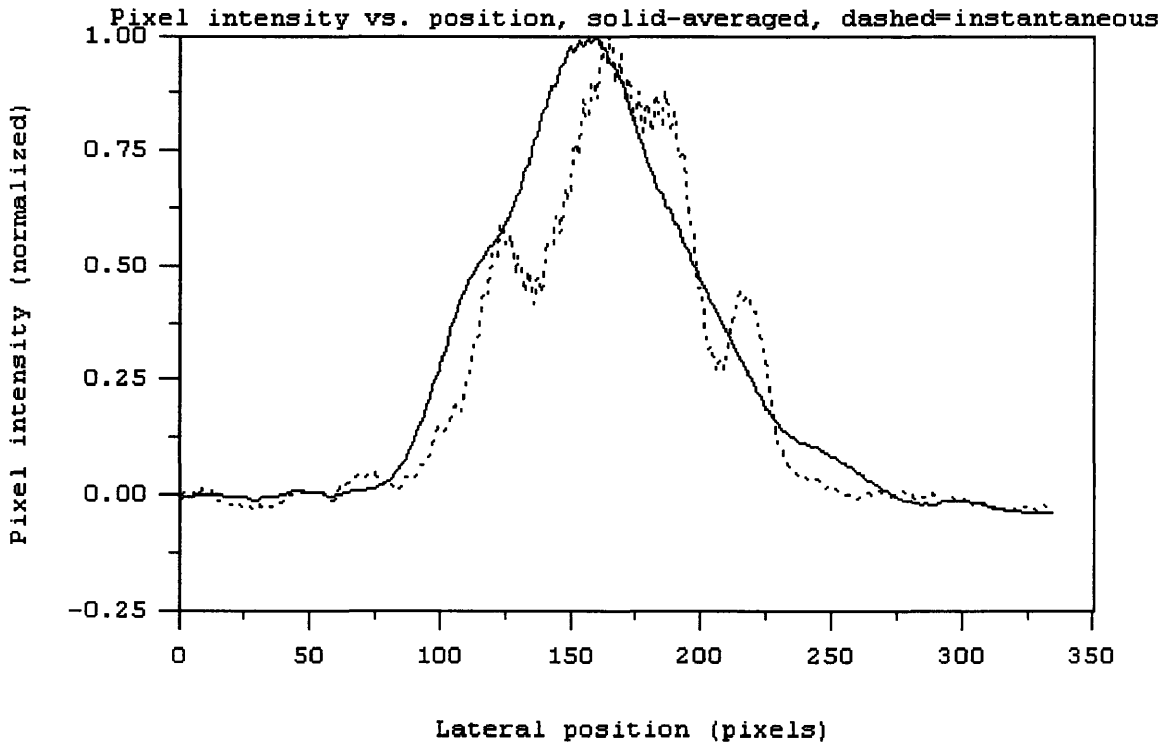

Figure 13: Comparison of instantaneous and averaged profiles

3 Results

3.1 Diffusion Coefficient

Thirty-two values of D were found, one for each of the cases investigated. The values for the lateral coefficient are in Table 3. As expected, the diffusion coefficient D_y increased with both velocity and dowel density. A similar effect was found in the vertical coefficient (Table 4).

Of particular interest to this study is the effect of dowel density, which turned out to be quite significant in both lateral and vertical diffusion (Figures 16 and 17).

The 6 cm/s and 3 cm/s cases for vertical diffusivity did not follow the same pattern as the others, but this may have been due to the effect of gravity. In the slower cases, the time scale for gravitational settling of the dye was comparable to the time scale for advection through the test area, so the dye cloud intersected with the bottom of the flume. This was corrected for by modeling it as if the dye cloud were perfectly reflected off the bottom, but that was a simplification of what was actually happening, since most of the dye which settled to the bottom stayed at the bottom. The compensation method did not

account very well for this dye which collected at the bottom, so the results were not necessarily accurate.

In both the lateral and vertical cases, the largest increase in diffusivity was seen between the null and low-density cases, which indicates that the presence of any dowels/plants causes a significant increase in mixing relative to the case with no dowels/plants. Also, the effect of the added dowels seemed to decrease with increased dowel density. This indicates that there is probably a maximum effect which the obstructions can have, with the level of mixing approaching an asymptote at that level.

Table 3: D_y, lateral coefficient (cm^2/s)

	3 cm/s	6 cm/s	9 cm/s	12 cm/s
Null	0.03±0.01	0.09±0.01	0.19±0.02	0.22±0.02
Low	0.26±0.05	0.55±0.06	0.72±0.21	0.6±0.23
Med	0.39±0.08	0.70±0.07	1.08±0.16	1.37±0.13
High	0.61±0.25	1.44±0.17	2.58±0.11	3.49±0.16

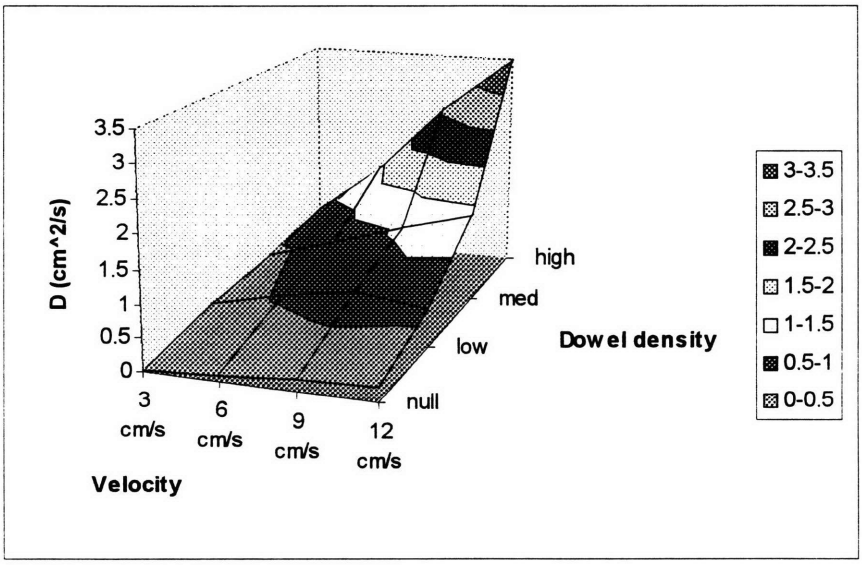

Figure 14: Results, lateral coefficient

Table 4: D_z, vertical coefficent (cm^2/s)

	3 cm/s	6 cm/s	9 cm/s	12 cm/s
Null	0.03±0.01	0.09±0.01	0.08±0.02	0.09±0.01
Low	0.09±0.02	0.09±0.04	0.25±0.08	0.24±0.03
Med	0.07±0.02	0.15±0.05	0.36±0.05	0.48±0.07
High	0.18±0.01	0.31±0.04	0.69±0.04	0.87±0.10

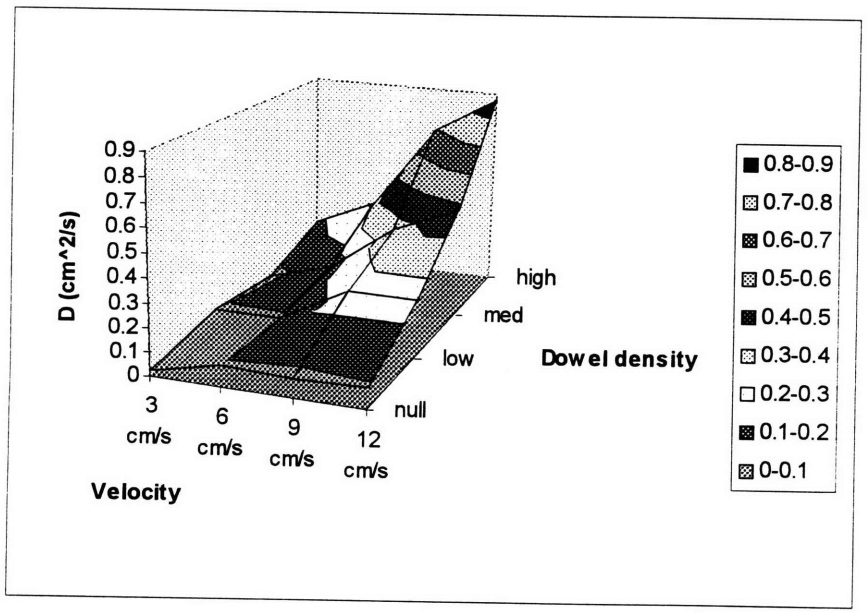

Figure 15: Results, vertical coefficient

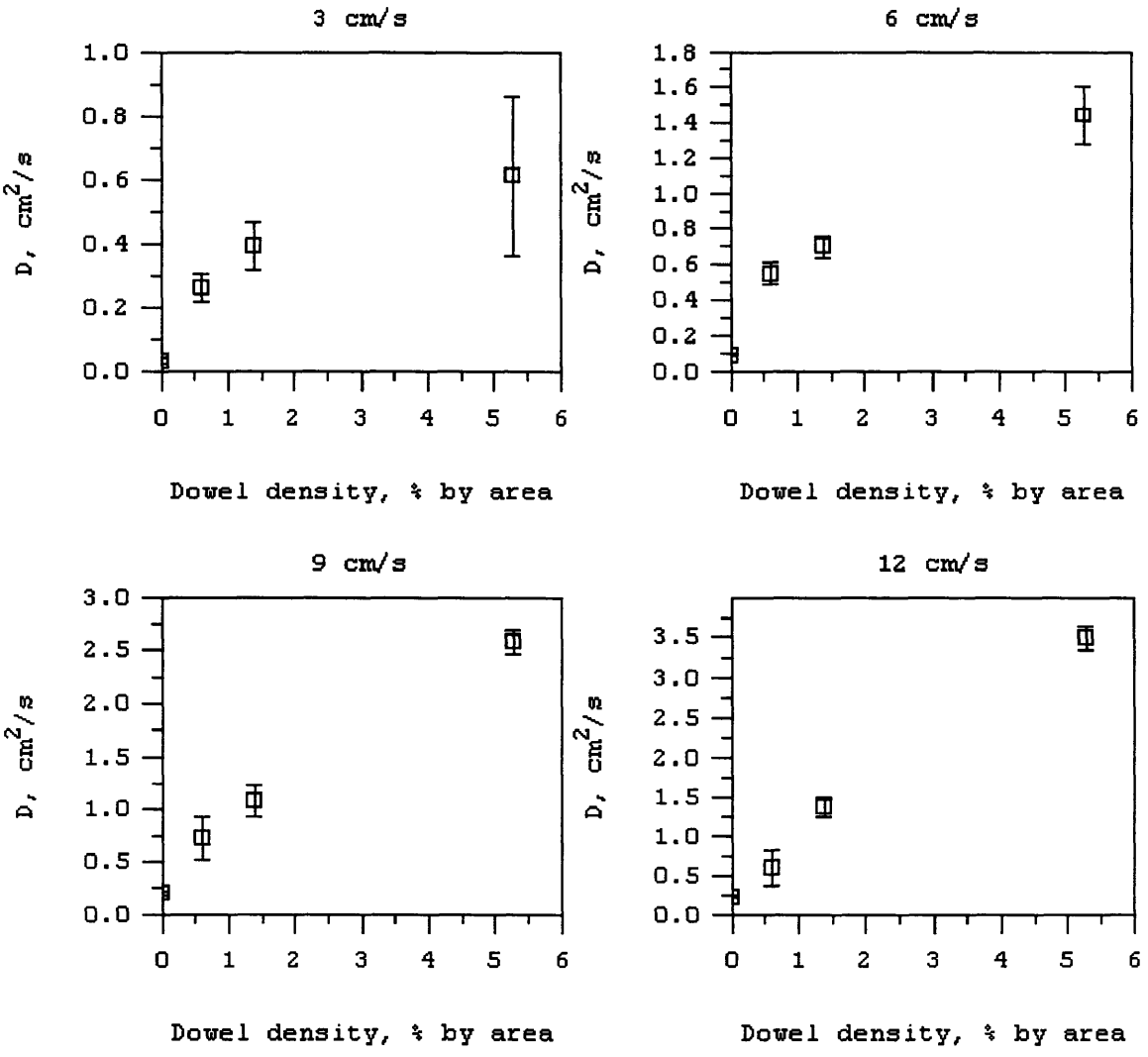

Figure 16: D vs. dowel density, lateral cases

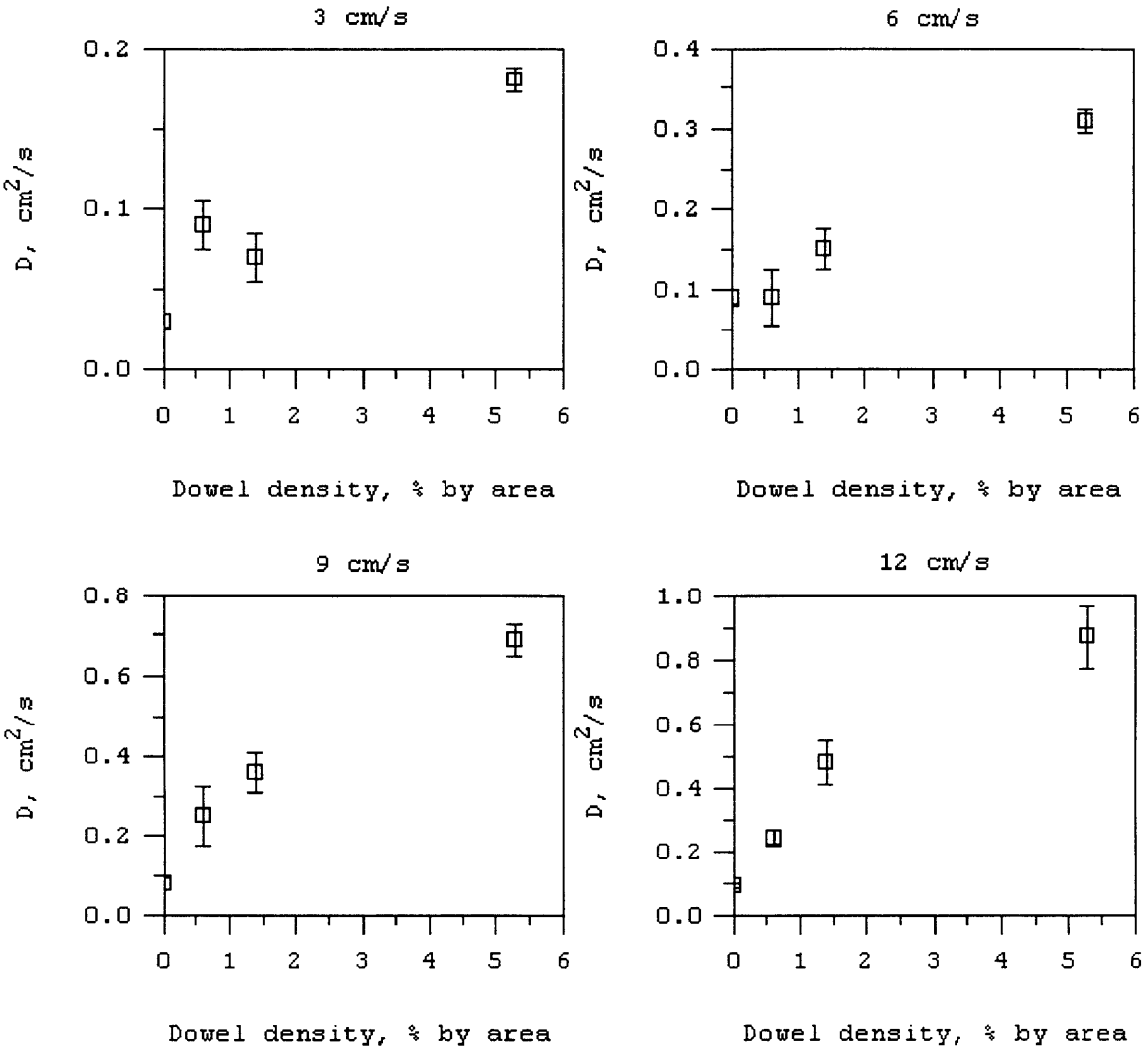

Figure 17: D vs. dowel density, vertical cases

3. 2 Small-scale mixing: C_{rms} data

Values of C_{rms} were found for all lateral cases (Table 5). By plotting these points against dowel density (Figure 18; see Table 5 for uncertainty of C_{rms} values) it can be seen that the dowels have a clear effect on C_{rms}. This indicates that the presence of the dowels causes much more small-scale mixing to happen within the dye plume, so that the dye concentration is more smoothly distributed on an instantaneous level. This corroborates the results of Anderson and Charters (1982), who found that large-scale turbulence was reduced within by the presence of aquatic plants, but small-scale turbulence was introduced. This effect can also be seen quite clearly in the images (Figures 19 and 20). In the null case photograph, the larger eddies are indicated by the bright, meandering streams of dye, while for the high-density case smaller eddies can be seen within a much more well-mixed plume.

Table 5: C_{rms}

	3 cm/s	6 cm/s	9 cm/s	12 cm/s
Null	0.27±0.10	0.50±0.07	0.52±0.07	0.29±0.10
Low	0.35±0.09	0.17±0.11	0.34±0.08	0.20±0.10
Med	0.32±0.08	0.22±0.9	0.12±0.11	0.13±0.11
High	0.14±0.10	0.11±0.11	0.16±0.12	0.16±0.11

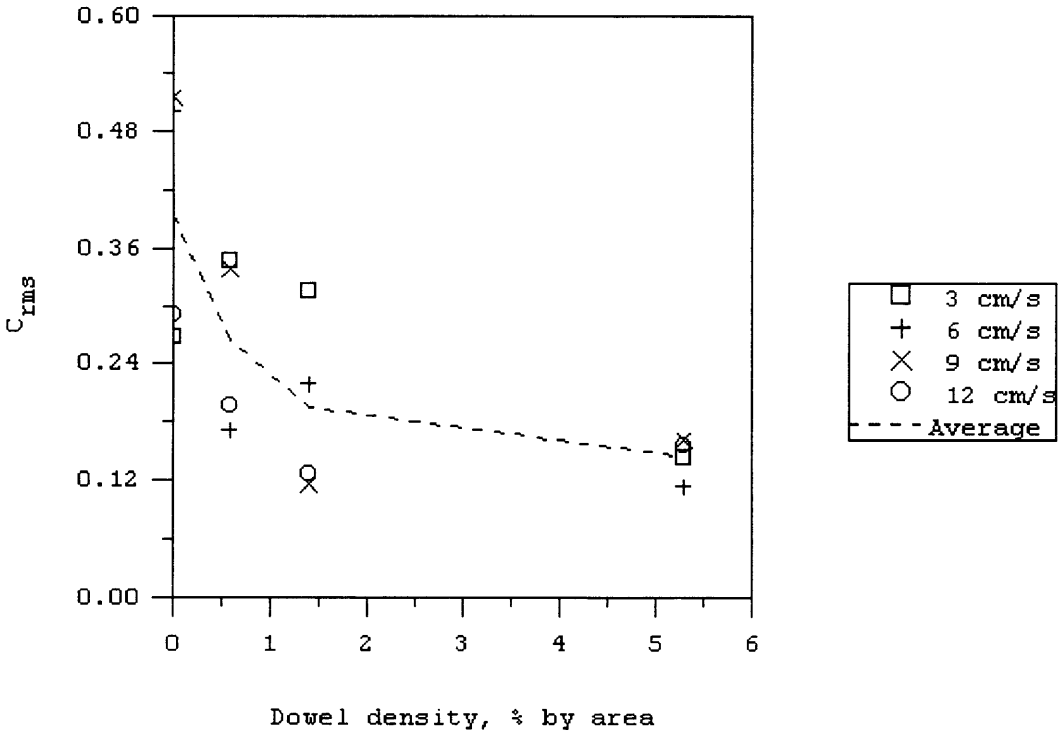

Figure 18: Crms vs. dowel density

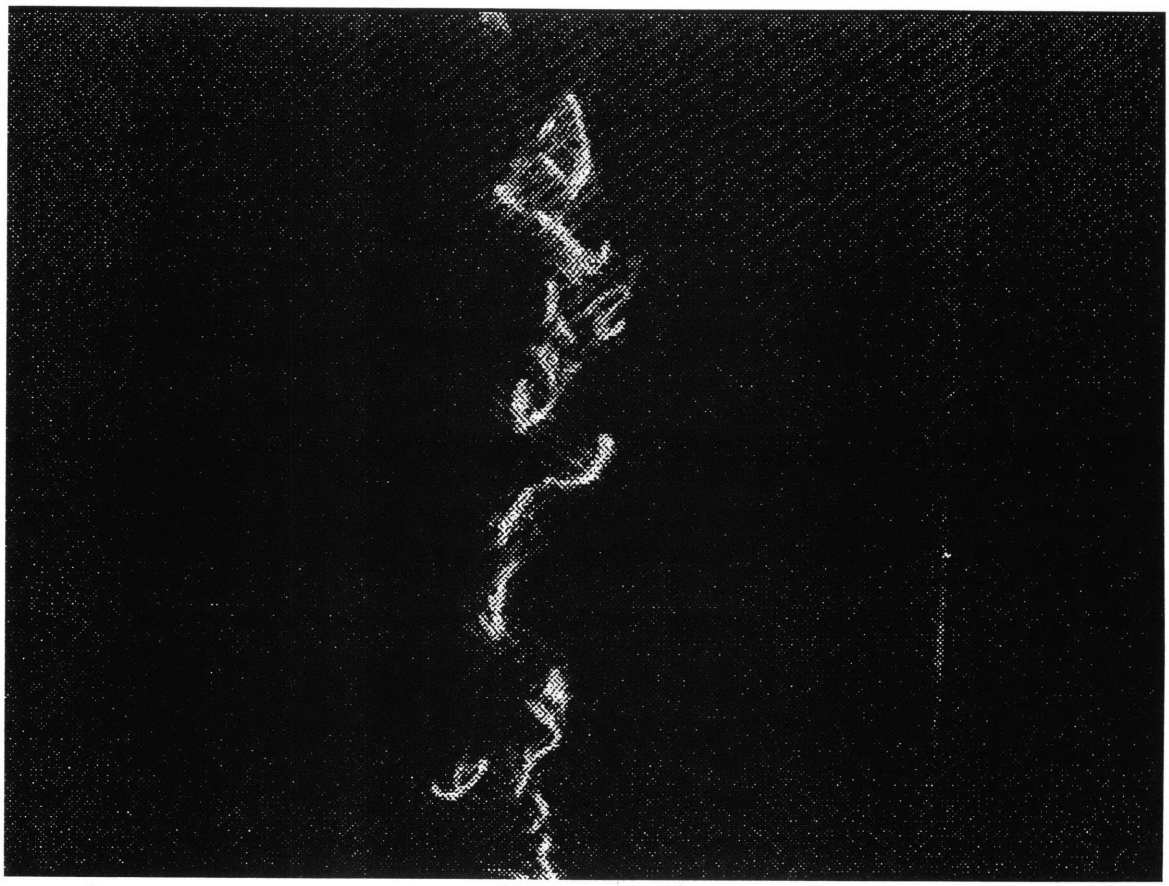

Figure 19: Instantaneous image, null case, 6 cm/s lateral

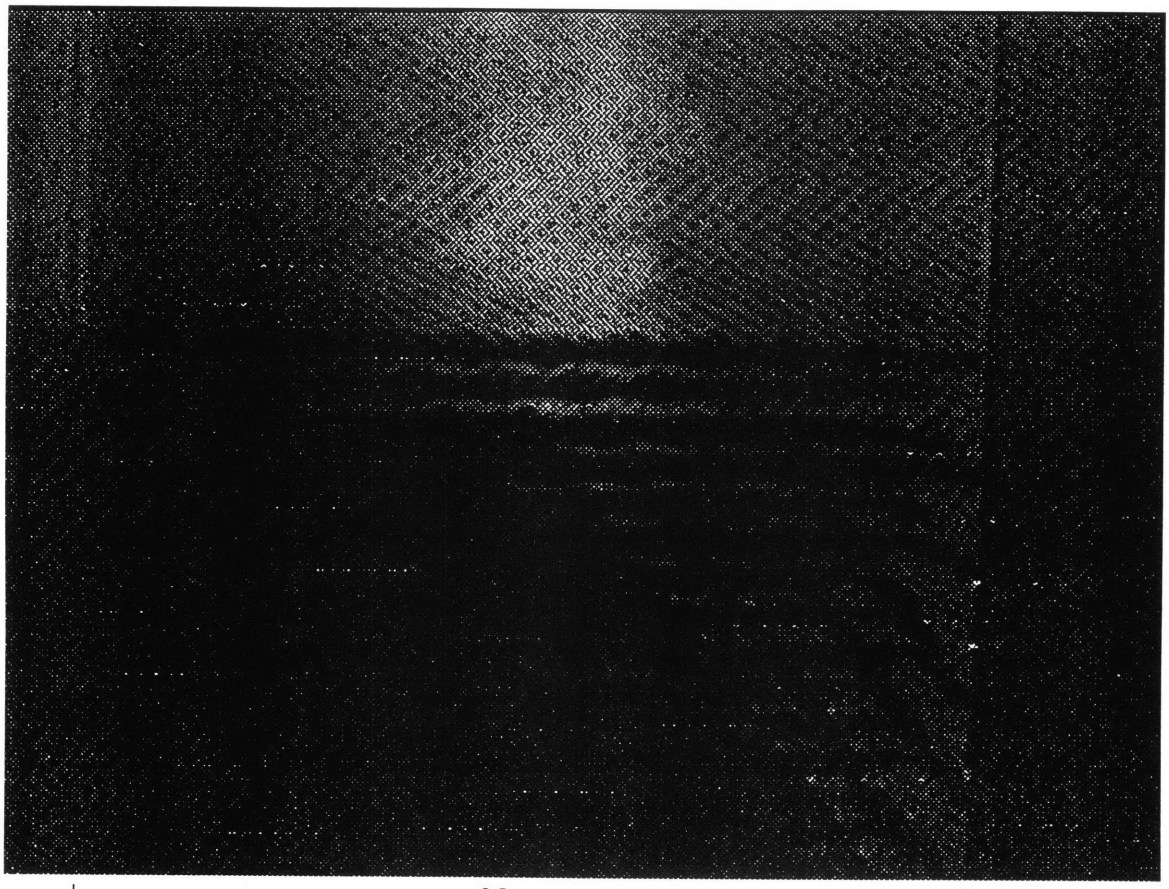

Figure 20: Instantaneous image, high density case, 6 cm/s lateral

4 Mechanical Model for Diffusion

4.1 Lateral Diffusivity: Theory

4.1.1 Probabilistic Theory

Based on the observations just described, the dowels/model plants have a large effect on diffusion. The most obvious reason for this is the effect of the wakes which develop behind the dowels as a result of vortex formation (Figure 21).

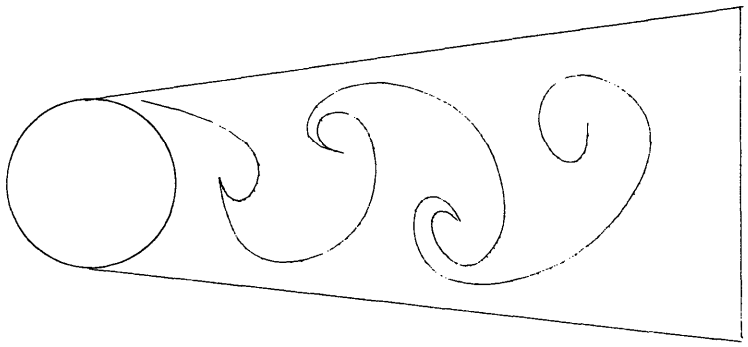

Figure 21: Wake region behind a dowel

In order to quantify the lateral wake effect, a theoretical model was derived based on a modification of the classic random walk model of diffusion, which describes mixing as random movement of particles over a series of time steps (Fischer et al 1979). While the original random walk model, as used to define molecular diffusion, assumes an equal probability of a particle's moving in any direction in any time step, here the model is modified by stating that the most significant source of lateral motion is encounter with a dowel, so a particle of dye has a probability of being shifted in the lateral direction equal to its probability of encountering a dowel or its wake region.

The probability of hitting a dowel or wake region at any one point is taken to be $\mathcal{D}^*$, the 'dowel wake density', or percentage by area of the flow region covered by dowels and wake regions. $\mathcal{D}^*$ is related to $\mathcal{D}$, the percentage by area covered by the dowels themselves ($\mathcal{D}$ is areal dowel density as defined in Section 2.1.3; a detailed description of how the relationship between $\mathcal{D}$ and $\mathcal{D}^*$ was modeled is provided in Section 4.1.2). When a particle hits a wake, it will move either to the left or to the right of the dowel/wake area with equal probability. It is assumed that the particle does not have a relatively significant lateral movement if it is outside of a wake region, an assumption which is validated by the fact that Zavistoski (1994) found that turbulence intensity within a wake was as much as twice that in wake-free regions.

Given this, the lateral movement of the dye in a given spatial step (illustrated in Figure 22) can be described by the probability distribution function:

(4.1.1) $P(dy = 0) = 1 - \mathcal{D}^*$ (particle a)

$P(dy = w) = \frac{\mathcal{D}^*}{2}$ (particle b)

$P(dy = -w) = \frac{\mathcal{D}^*}{2}$ (particle c)

This distribution has a mean of 0:

(4.1.2) $$\mu = \sum xf(x) = 0(1 - \mathcal{D}^*) + w\frac{\mathcal{D}^*}{2} + -w\frac{\mathcal{D}^*}{2} = 0$$

and standard deviation $w^2\mathcal{D}^*$:

(4.1.3) $$\sigma^2 = \sum (x - \mu)^2 f(x)$$

$$= (0-0)^2(1 - \mathcal{D}^*) + (w-0)^2\frac{\mathcal{D}^*}{2} + (-w-0)^2\frac{\mathcal{D}^*}{2} = w^2\mathcal{D}^*$$

By the central limit theorem the distribution of lateral particle positions after this process occurs N times is a Gaussian distribution with mean 0 and standard deviation $\sigma^2 = N\mathcal{D}^* w^2$ (Hogg and Tanis 1993).

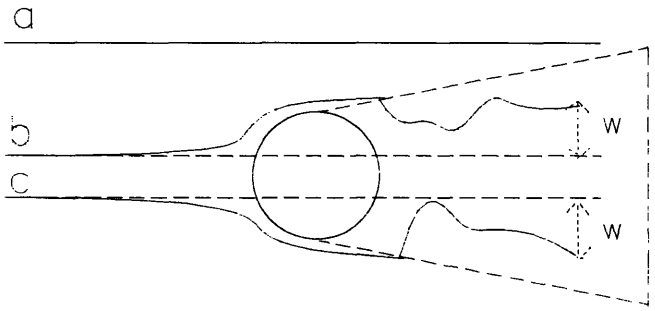

Figure 22: Possible interactions of dye particle with dowel

A value of D_y, the diffusion coefficient as a result of this effect, can be determined using the formula:

$$D_y = \frac{1}{2}\frac{\sigma_y^2}{t} = \frac{1}{2}\frac{N\delta' w^2}{t} \qquad (4.1.4)$$

Since velocity and distance traveled within the array are known values, t can be taken to be x/u.

According to Hinze (1975), the mixing coefficient within a dowel wake, D_{wake}, scales on the velocity and the size of the obstruction:

$$D_{wake} \sim ud \qquad (4.1.5)$$

From this relationship, it can be seen that for a time step Δt, the lateral mixing distance is:

$$w \sim \sqrt{D_{wake}\Delta t} = \sqrt{ud\left(\frac{d}{u}\right)} = d \qquad (4.1.6)$$

Δy is the same as w, so this means that $w=d$.

An appropriate spatial step to use in determining the number of steps N is the length of a dowel diameter, since it is a large enough step so that a particle will not encounter the same dowel twice in one step, yet small enough so no more than one dowel will be hit by the same particle in a step, making this model valid. Using this as the spatial step, N becomes equal to x/d, the total length traveled within the array divided by dowel diameter. Combining all of these characteristics with Equation 4.1.4 produces the result:

$$D_y = \frac{1}{2}\delta^* ud \qquad (4.1.7)$$

Thus, the diffusion coefficient is a function of dowel wake density, dowel diameter, and velocity.

4.1.2 Definition of δ^*, dowel wake density

Since d and u are known quantities, the only parameter which has yet to be defined is δ^*. δ^* is related to δ, the dowel density percentage, but cannot be assumed a direct multiple of δ because of overlap of wake regions. At very low densities where the dowels are not close enough together to interact, δ^* is a multiple of δ, because each dowel's wake fully develops in the same manner as in a single-dowel case (see Figure 23 for a depiction of how this might look). On the other hand, when the dowel density is higher, the wakes from the different dowels overlap (Figure 24). Thus, the proportion of wake region to dowel region becomes lower as the dowel region increases.

This effect was modeled by using Matlab to produce a grid with randomly spaced 1x1 'dowels' and modeling the wake region for each of these dowels to determine the average overlap and its effect on δ^* (See Appendix 2 for the Matlab m-file used in this process). The wake ratio (ratio of wake size:dowel size) was varied to get different curves (Figure 25), and these various curves were later compared to the data results to see which wake size worked best. In all cases, the proportion of increase in wake area to increase in dowel area decreases as the dowel area becomes larger, moving toward an

asymptote of 1, since the largest possible wake area fraction is 100%. As expected, the wake area fraction approaches 1 faster for larger wake sizes.

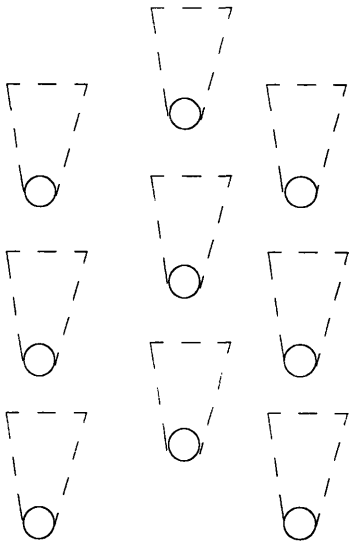

Figure 23: Low wake interaction

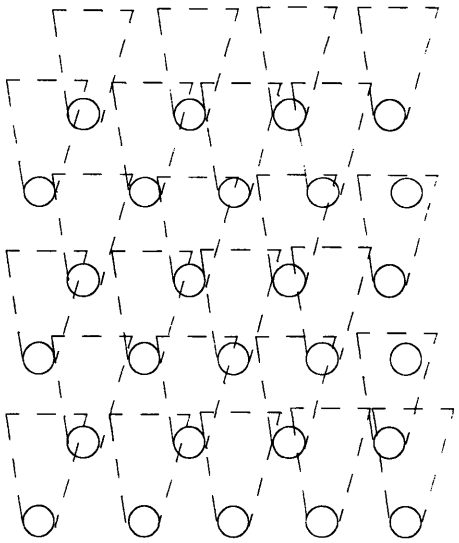

Figure 24: High wake interaction

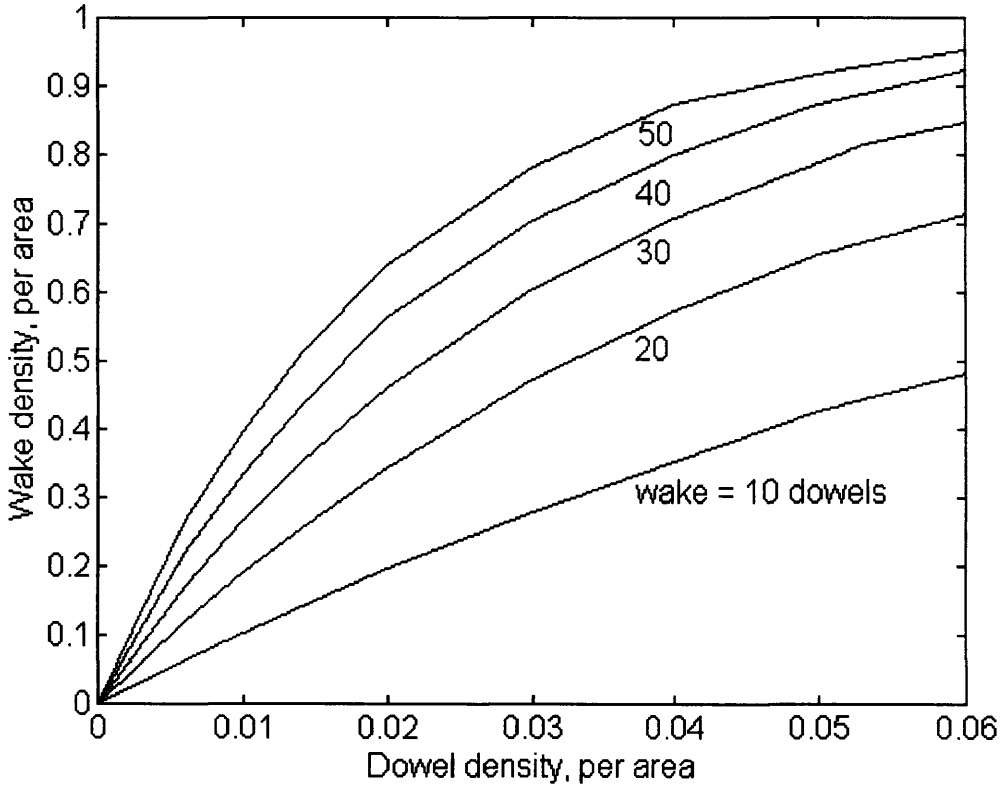

Figure 25: Variation of wake fraction with dowel fraction

The optimum value of wake size was determined by comparing the theoretical curves for different wake sizes to the experimental data.

For this and the following analyses of the results, all experimental values of D were normalized as follows to make it easier to compare them to the theory. First, the

value actually used for D was D-D_{null}. This value was used because by subtracting out ambient diffusion, the diffusion that resulted from the plants could be isolated. Also, for this case, the values of D were normalized by multiplying by $2/ud$, to get the corresponding value of δ^* for the theoretical model:

$$D = \frac{1}{2}\delta^* ud, \text{ so} \tag{4.1.8}$$

$$\delta^* = \frac{2D}{ud} \tag{4.1.9}$$

This was done so that the data could be directly compared to the δ^* curves obtained from the Matlab program.

To determine the value of the wake size, the normalized data points were compared to the corresponding points on the theoretical curve and the root mean square of the differences between the data and theoretical points was minimized, in a manner similar to the method of matching the pixel intensity data to Gaussian distributions. By this method, it was determined that the best fit was for a wake 24 times the size of the dowel (rms difference=0.07), although ratios ranging from 18 to 35 gave values of rms difference less than 0.1, so any value in this range is a potential match (Figure 26). This value of wake:dowel size ratio is the same order of magnitude as some of the wake depictions in previous studies (i.e. Meroney 1968, Zavistoski 1994) indicate, but no previous measurements of wake size were found which were precise enough for a numerical comparison.

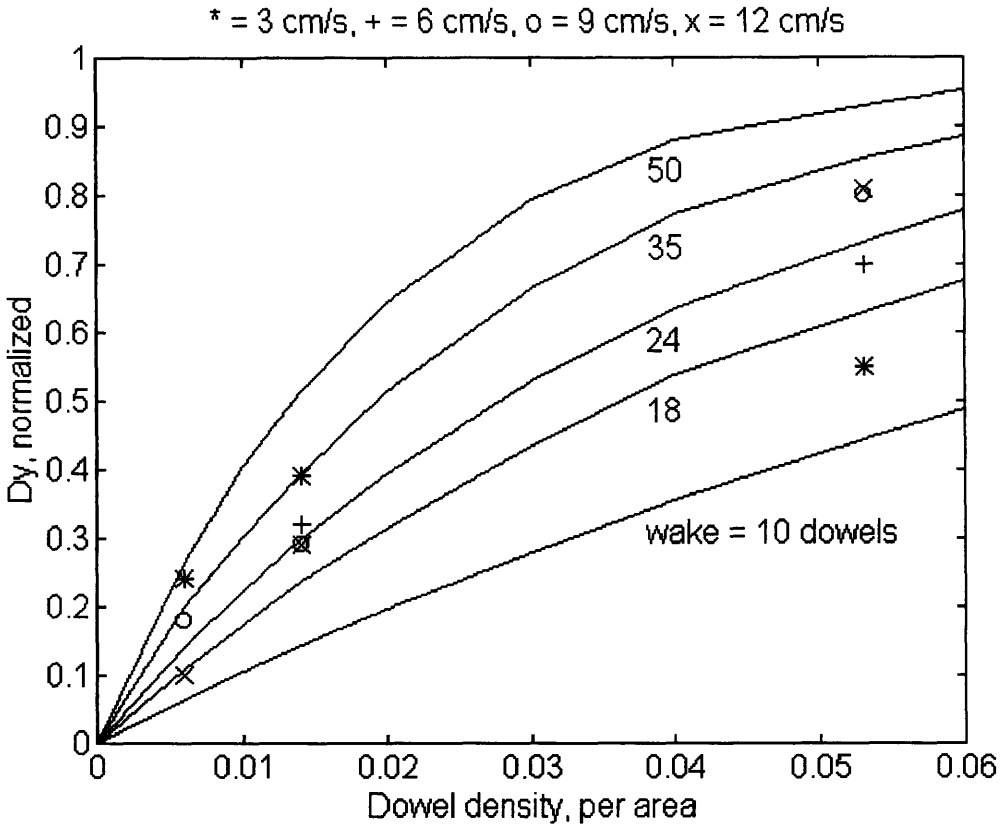

Figure 26: Comparison of different theoretical curves to data

4.1.3 Evidence of validity of model

Based on Equation 4.1.5, it can easily be shown that D_y, as defined by the model, is a direct multiple of the dowel Reynolds number of the flow times the wake density:

$$D_y = \frac{1}{2} \delta^* ud = \frac{1}{2} \nu \delta^* \mathrm{Re}_d \tag{4.1.10}$$

where ν is the kinematic viscosity of water, a constant. ν=0.01, so this actually becomes

$$D_y = 0.005 \delta^* \mathrm{Re}_d \tag{4.1.11}$$

The validity of this result can be seen by plotting the data results for D_y against $\delta^* \mathrm{Re}_d$ (Figure 27). The plotting software was used to determine the best linear fit for the data, which is a line of slope 0.0054 and y-intercept -0.016.

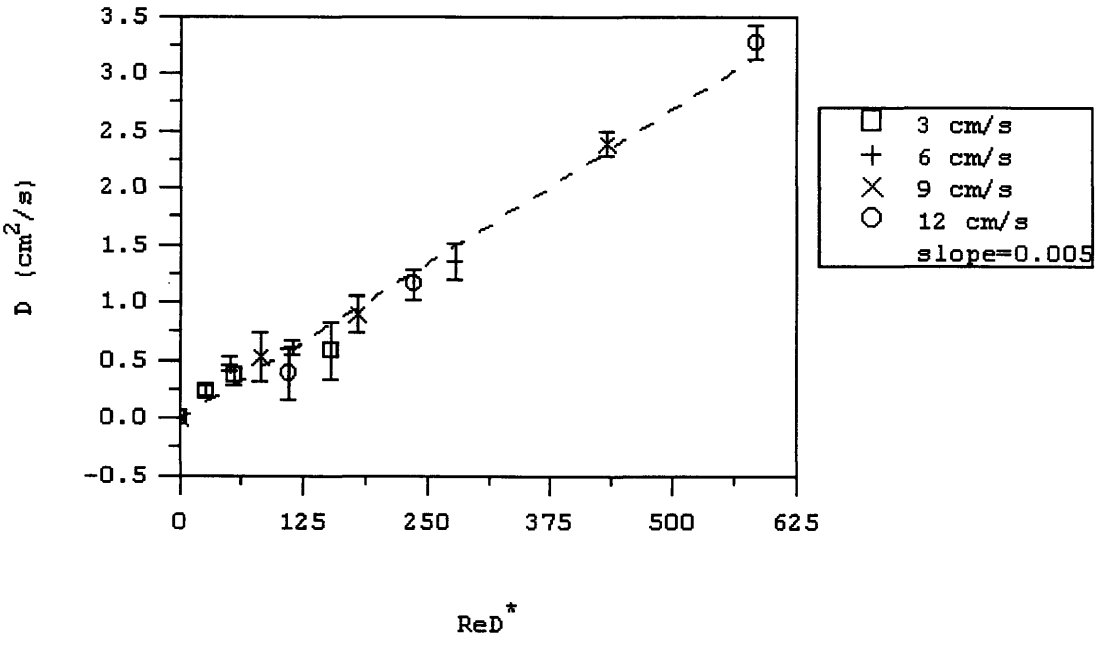

Figure 27: Linear relationship between D and $\delta^* \mathrm{Re}_d$

A second way in which the model can be verified is by noticing that that in this model it is assumed that the wake ratio is not a function of Reynolds number. This means that δ^* is not taken to be a function of velocity. Thus, this assumption says that the width

to which a dye stream spreads is not a function of velocity, but only depends on the size and number of dowels/plants encountered. This prediction can be confirmed by determining the value of σ^2 (the standard deviation of the Gaussian distribution, a measure of width) for each experimentally determined D_y ($\sigma_x^2 = 2D_x t$) and plotting that against the velocity. The uncertainty of the values of σ^2 is determined by combining the uncertainty of D and the uncertainty of the velocity (taken to be 2 mm/s) using the "constant odds" method of Kline & McClintock (1953):

$$E_{total} = \sqrt{(\frac{\partial \sigma^2}{\partial D} E_D)^2 + (\frac{\partial \sigma^2}{\partial u} E_u)^2} \qquad (4.1.12)$$

Using the above definition of σ^2, we get:

$$\frac{\partial \sigma^2}{\partial D} = 2Dt \qquad (4.1.13)$$

and

$$\frac{\partial \sigma^2}{\partial u} = -0.4\, cm/s\, D\frac{t}{u} \qquad (4.1.14)$$

so:

$$E_{total} = \sqrt{(2tE_D)^2 + (\frac{-0.4cm/s\, Dx}{u^2})^2} \qquad (4.1.15)$$

The results and uncertainty of this analysis are in Table 6, and the values are plotted in Figure 28. This plot shows that spreading width is fairly constant relative to velocity, which indicates that the assumption that velocity does not affect the width of the plume is correct.

Table 6: σ^2 (Plume width)

	3 cm/s	6 cm/s	9 cm/s	12 cm/s
Null	0.79±0.21	1.01±0.12	1.17±0.15	1.07±0.08
Low	2.42±1.08	2.50±0.71	2.15±1.35	1.80±1.22
Med	3.05±1.88	2.82±0.78	2.79±1.13	2.72±0.68
High	3.54±5.20	3.98±1.88	4.00±0.73	4.01±0.75

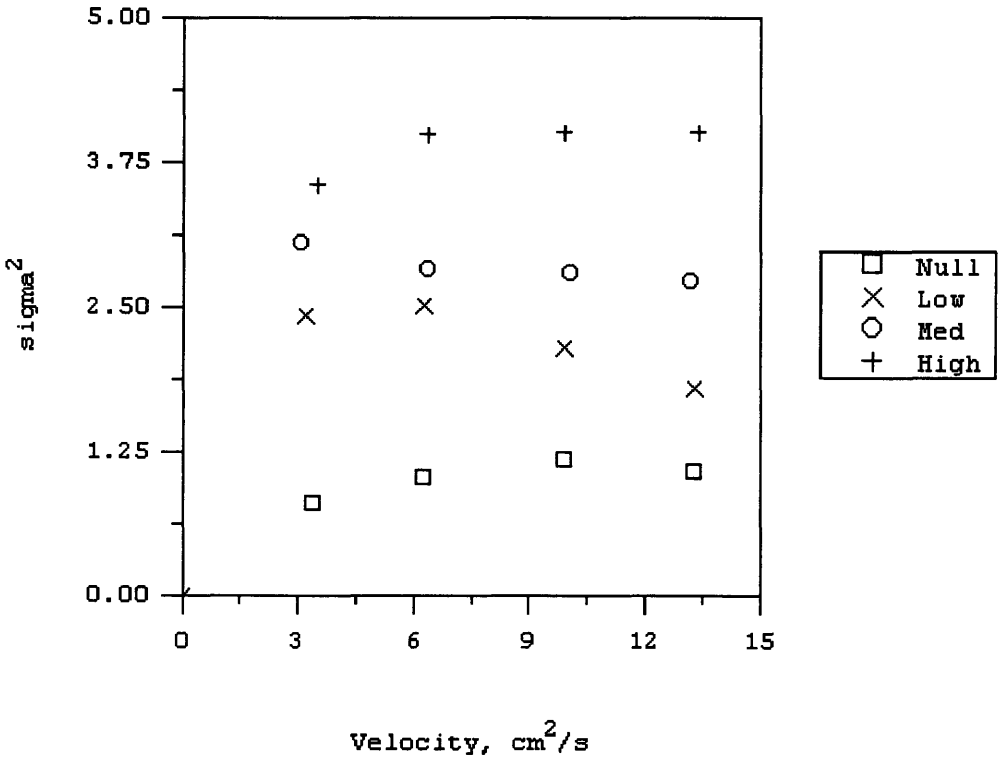

Figure 28: Effect of velocity on width of dye plume

4.2 Lateral Diffusivity: Comparison to Data

The normalized experimental values of D_y are compared to the values of δ^* determined by the Matlab model in Figure 29.

Uncertainty is recalculated for the normalized results, to account for both the uncertainty of the match to the theoretical curve and that associated with the velocity measurements, which were used in normalizing the data. Once again, the error of the ADV is taken to be 2 mm/s, and the two sources of error are combined using the constant odds method:

$$E_{total} = \sqrt{(\frac{\partial D_n}{\partial D} E_D)^2 + (\frac{\partial D_n}{\partial u} E_u)^2} \tag{4.2.1}$$

$$D_n = \frac{2D}{ud} \tag{4.2.2}$$

$$\frac{\partial D_n}{\partial D} = \frac{2}{ud} \tag{4.2.3}$$

$$\frac{\partial D_n}{\partial u} = -\frac{2D}{u^2 d} \tag{4.2.4}$$

$$E_{total} = \sqrt{(\frac{2E_D}{ud})^2 + (\frac{-0.4cm/s D}{u^2 d})^2} \tag{4.2.5}$$

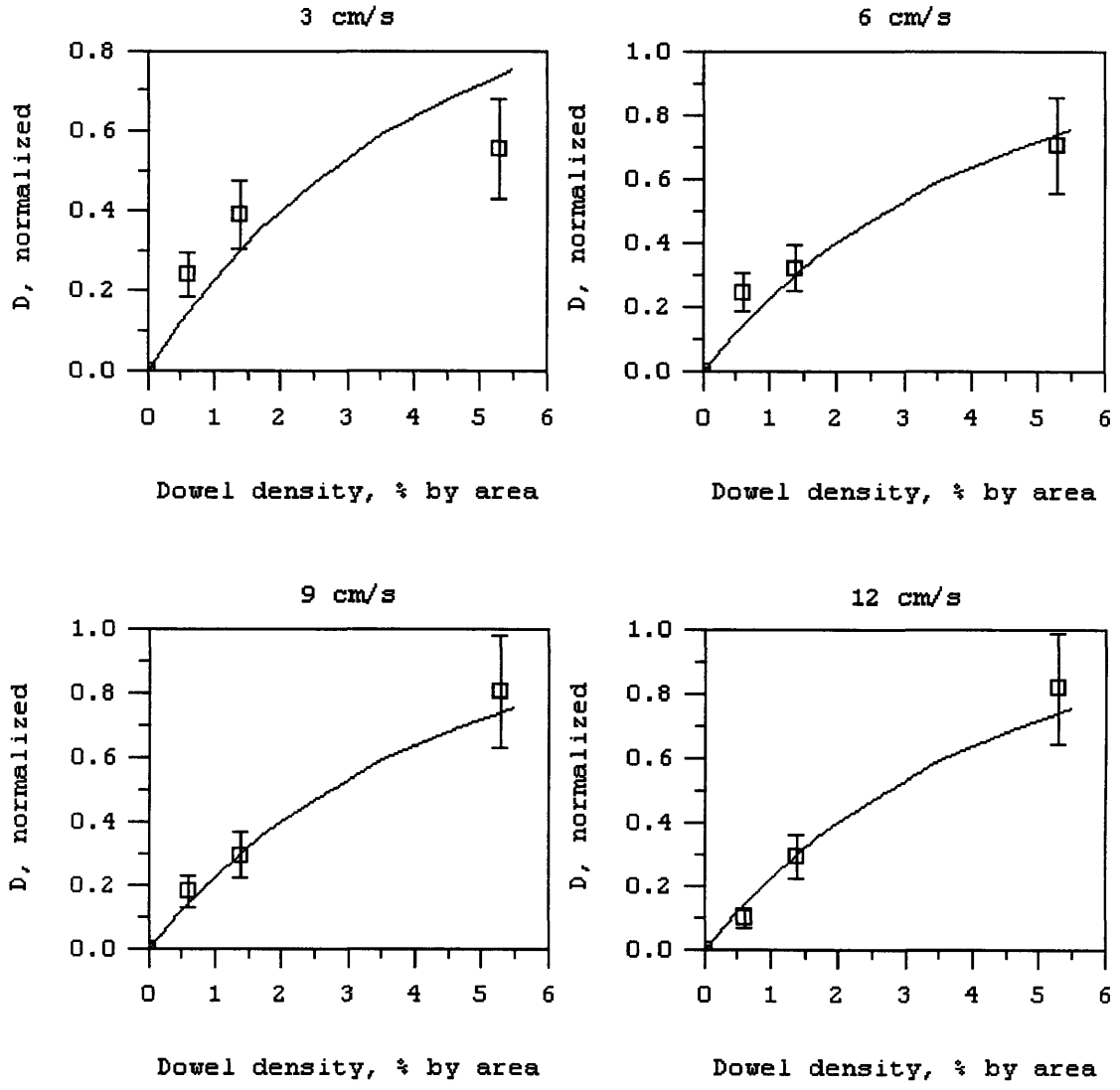

Figure 29: Comparison of experimental results to theory, lateral diffusivity

In order to see how the model holds up for a different size of dowel, the results of another experiment using 1.2 cm diameter dowels are also compared to the theoretical curve (Figure 30). This experiment was performed by an undergraduate lab class under the direction of Heidi Nepf. These data points also fit well to the theoretical model, indicating that the model can be used for different sizes of plants.

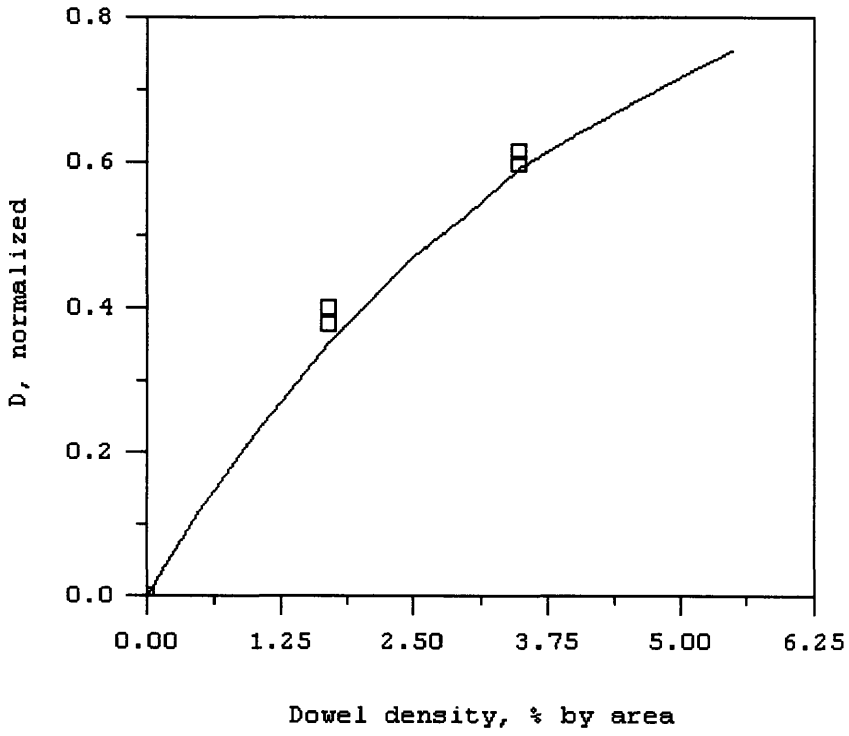

Figure 30: Comparison of student lab results to theory

4.3 Vertical Diffusivity

The effect of the dowels on vertical mixing is more difficult to define than the effect on lateral mixing, because there are additional processes involved. In addition to the immediate effect of impact with the dowel or wake region, which is itself not well-understood, there are also pressure effects to be taken into account.

Stagnation pressure is caused by the encounter of flowing water with a stationary object. The corresponding decrease in pressure on the other side of the obstruction is called recovery pressure. Because the velocity profile in the flume causes velocity to be higher at the top of the water than at the bottom, these pressures are different at the top and bottom of the dowel. Just upstream of the dowel, stagnation pressure is higher at the top, causing downward flow. Likewise, just downstream of the dowel pressure is lower at the top, causing upward flow (Zavistoski 1994). See Figure 31 for a conceptual representation of this process.

A preliminary flow visualization study found that the most noticeable effect was the updraft behind the dowel. Dye injected at the bottom of the flume rose about 7 cm. There was little effect of velocity on rise height, except in the fastest (12 cm/s) velocity, when the height was about 6 cm.

This vertical velocity may have a significant effect on mixing rates for some cases. A comparison of order-of-magnitude estimates of the time scales for turnover by vertical velocity

$$T_{turnover} = \frac{h_{rise}}{v_{rise}} \qquad (4.3.1)$$

and by diffusion

$$T_{turnover} = \frac{h_{rise}^{\ 2}}{D_z} \qquad (4.3.2)$$

was performed based on Zavistoski's data for updraft velocity at a streamwise velocity of 6 cm/s (Table 7). The results show that the relative significance of the two processes may change with changes in density. While the time scale for vertical velocity is significantly larger for the low and medium density cases, for the high density case both effects are the same order of magnitude, indicating that the updraft velocity effect may be significant to the mixing process.

Table 7 Time scales of updraft velocity and diffusion

Density	$T_{velocity}$	$T_{diffusion}$
Low	1900	540
Medium	1700	330
High	440	160

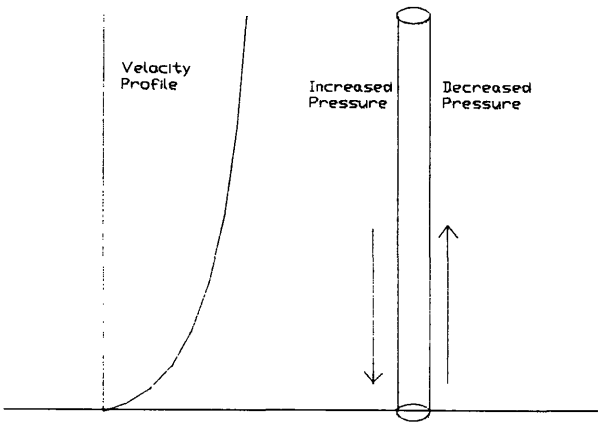

Figure 31: Vertical transport due to dowel pressure effects

It is, however, reasonable to assume that encounters with dowels and wakes have some effect on vertical diffusion, which would mean that the shape of the resulting theoretical curve would be similar to the one used in the lateral theory, although the magnitude might be different due to the different mixing scales involved. By plotting D_z against D_y (Figure 32), it can be seen that $D_z \cong 1/4 D_y$ (the actual best-fit line is $y = 0.248x + 0.032$).

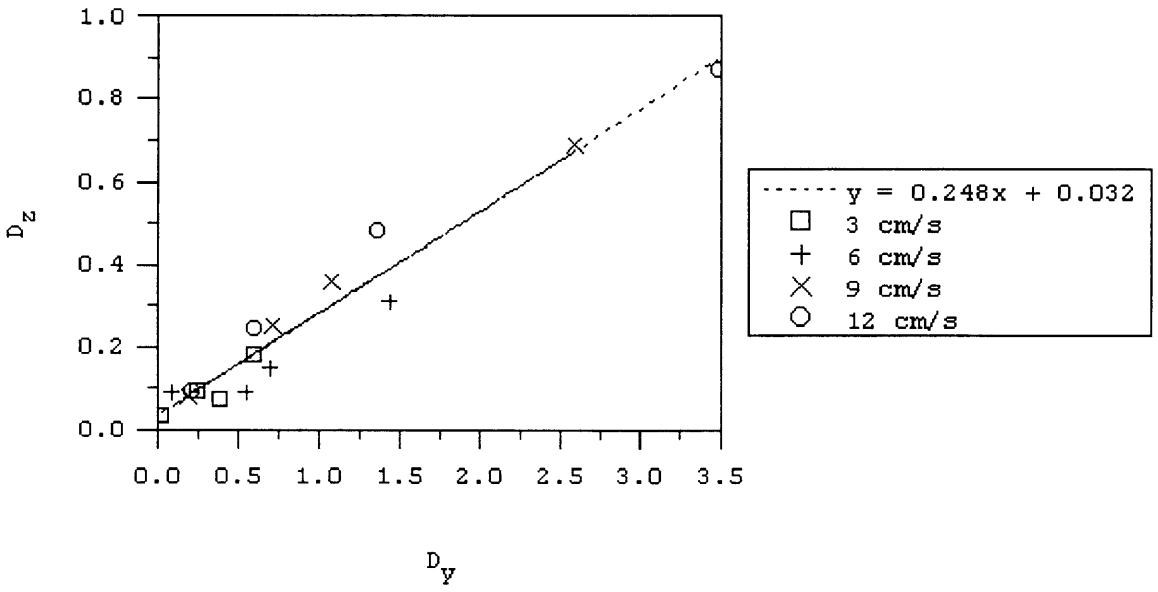

Figure 32: Comparison of magnitude of vertical and lateral diffusivities

It can easily be shown that this means that w_z, the vertical distance mixed in an encounter, is $1/2 w_y = 1/2\ d$:

$$D_z = \frac{1}{4} D_y \qquad (4.3.3)$$

$$\frac{1}{2}\frac{\mathcal{S}^* w_z^{\,2} u}{d} = \frac{1}{4}\left(\frac{1}{2}\frac{\mathcal{S}^* w_y^{\,2} u}{d}\right) \tag{4.3.4}$$

$$w_z^{\,2} = \frac{1}{4} w_y^{\,2} \tag{4.3.5}$$

$$w_z = \frac{1}{2} w_y = \frac{1}{2} d \tag{4.3.6}$$

This gives

$$D_z = \frac{1}{8}\mathcal{S}^* du \tag{4.3.7}$$

so the vertical data can be normalized by multiplying by 8/*ud* and compared directly to the same $\mathcal{S}^*$ estimate used for the lateral data. This also increases the magnitude of the uncertainty. It can be seen from this graph that the shape of the $\mathcal{S}^*$ curve does indeed predict the vertical data points (Figure 33). The slower velocities do not match the theory very well, probably because of error in the fitting process due to the gravity effect mentioned earlier.

The match between the vertical data and the shape of the theoretical curve indicates that, although it is uncertain what the dominant processes are within the wake, wake processes are causing a significant amount of the vertical mixing. Since it is unkown what processes are dominating, it is not understood at this point why the vertical mixing scale is 1/2 the lateral scale, so it is unclear whether that parameter is generalizable or not. The specific nature of the vertical mixing processes occurring within the wake would be an interesting subject for future study.

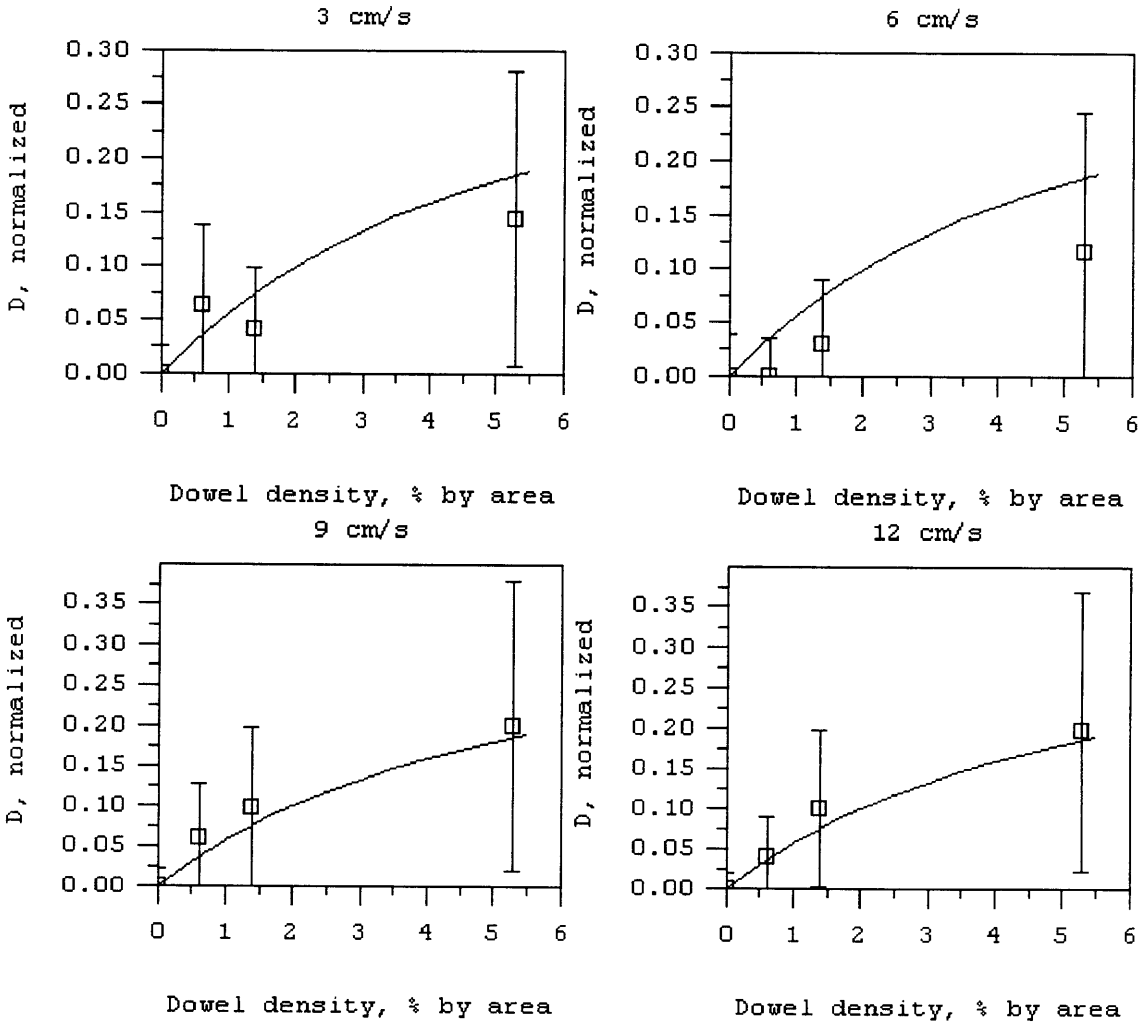

Figure 33: Comparison of vertical data to theory

5 Conclusions and recommendations

5.1 Conclusions

The results of this experiment indicate that lateral and vertical mixing are indeed greatly enhanced relative to free-stream flow of the same velocity by the presence of vegetation-like obstructions. A basic mechanical model describes the general effect of such obstructions on flow. The model is particularly useful because, being based on simple principles, it can be modified to describe other situations involving flow around fairly rigid, cylindrical, surface-piercing obstructions. In addition to being useful for estimating flow through *Spartina alterniflora*, it is applicable to analysis of situations involving water flow through trees, shrubs and other types of aquatic vegetation.

5.1.1 Natural wetland processes

The effects described here may play a significant role in the wetland ecosystem. Increased within-canopy mixing causes increased distribution of nutrients within the bed,

assisting the plants in uptake of such nutrients. It also leads to incrased distribution of pollen and seeds, which can enhance the plants' reproduction rate, thus aiding in maintenance and growth of the plant bed.

The recruitment and growth of other organisms is also affected by these mixing processes. Increased within-bed turbulence can cause a wider distribution of passive organisms and larvae within the canopy, in addition to distributing food to benthic filter-feeders and other organisms.

5.1.2 Constructed wetland design

In addition to their importance to natural wetlands, the mixing effects described here may be significant to the design of constructed wetlands. The rate of diffusion within vegetation has a significant effect on the rate at which wastewater entering a wetland is diluted to less harmful concentrations. It also affects the distribution of chemicals or other contaminants within the wetland, an effect which is quite important in wetland design because the distribution of wastes within the plant bed affects the rates of absorption or settling of contaminants, processes which artificial wetland designers would want to maximize.

By comparing the results of this study with the results from other studies it can be seen that there is real significance to the amount, type, and placement of vegetation in a constructed wetland. The fact that mixing was found to be increased within the plant bed in this flume experiment, as opposed to earlier findings of decreased mixing relative to

nearby open-water flow (i.e. Leonard and Luther 1995), shows that there is a significant difference between channelized flow around vegetation and flow which actually passes through the vegetation. Likewise, the results of this study also indicate that flow through surface-piercing vegetation differs greatly from flow in situations where the water can flow over the vegetation (i.e. the study by Gambi et al 1990). Both of these results indicate that the placement and type of vegetation has important hydrodynamic consequences.

Another factor which may be important to wetland design is density of plant beds. The model described here indicates that mixing rates are increased with increased stem density up to a certain point after which the effect reaches an upper limit. This fact could also be useful to constructed wetland designers in deciding what types of vegetation and planting patterns to use.

5.2 Recommendations for further study

This study provides a basic understanding of flow around vegetation based on a simplified model. Hopefully these results can be applied to studies incorporating some of the other effects not examined here. The effects of different types plant morphologies, such as plants with leaves or flexible plants, deserves further study. Further laboratory or field studies, in addition to more detailed analytical work, will make the various effects of different types of vegetation clearer.

Also, a closer look at the effects of stem wakes on vertical diffusivity would prove interesting. The results presented here indicate that wake processes are a significant source of vertical mixing, but it is unclear from this study what processes are most significant within the wakes and why the scale of vertical mixing is smaller than that of lateral mixing.

In addition, knowing some of the effects of vegetation poses the question of the role these effects play in the wetland ecosystem, such as in the recruitment and growth of different types of life or in the overall filtering capacity of a wetland. Further understanding of how processes such as those described here affect overall wetland function are essential to understanding the functioning of natural wetlands.

This increased understanding of wetland function can also be applied to wetland construction and restoration. Another area of further study could be the feasibility and effectiveness of applying the hydrodynamic principles discussed here to wetland design.

References

Ackerman, J.D. 1986. Mechanistic implications for pollination in the marine angiosperm *Zostera marina*. *Aquatic Botany* 24, 343-353.

Ackerman, J.D., and A. Okubo. 1993. Reduced mixing in a marine macrophyte canopy. *Functional Ecology* 4, 305-309.

Anderson, S.M. and A.C. Charters. 1982. A fluid dynamics study of seawater flow through *Gelidium nudifrons*. *Limnology and Oceanography* 27(3), 399-412.

Braza, M., P. Chassaing and H. Ha Minh. 1986. Numerical study and physical analysis of the pressure and velocity fields in the near wake of a circular cylinder. *Journal of Fluid Mechanics* 165, 79-130.

Brueske, C.C. and G.W. Barrett. 1994. Effects of vegetation and hydrologic load on sedimentation patterns in experimental wetland ecosystems. *Ecological Engineering* 3, 429-447.

Coutanceau, M. and J-R. Defaye. 1991. Circular cylinder wake configurations: A flow visualization survey. *Applied Mechanics Review* 44(6), 225.

Eckman, J.E. 1983. Hydrodynamic processes affecting benthic recruitment. *Limnology and Oceanography* 28(2), 241-257.

Elliott, D.L., and J.C. Barnard. 1990. Effects of trees on wind flow variability and turbulence. *Transactions of the American Society of Mechanical Engineers* 112, 320-325.

Fennessey, M.S., C.C.. Brueske, and W.J. Mitsch. 1994. Sediment deposition patterns in restored freshwater wetlands using sediment traps. *Ecological Engineering* 3, 409-428.

Fischer, H.B., E.J. List, R.C.Y. Koh, J. Imberger, and N.H. Brooks. 1979. Mixing in inland and coastal waters. Academic Press, New York.

Gambi, M.C., A.R.M. Nowell, and P.A. Jumars. 1990. Flume observations on flow dynamics in *Zostera marina* (eelgrass) beds. *Marine Ecology Progress Series* 61, 159-169.

Higuchi, H., H.J. Kim, and C. Farell. 1989. On flow separation and reattachment around a circular cylinder at critical Reynolds numbers. *Journal of Fluid Mechanics* 200, 149-171.

Hinze, J.O. 1975. Turbulence. McGraw-Hill, New York.

Hogg, R.V. and E.A. Tanis. 1993. Probability and statistical inference. Macmillan Publishing Company, New York.

Jacobs, A.F.G., J.H. van Boxel, and R.M.M. El-Kilani. 1995. Vertical and horizontal distribution of wind speed and air temperature in a dense vegetation canopy. *Journal of Hydrology* 166, 313-326.

Kadlec, R.H. 1990. Overland flow in wetlands: vegetation resistance. *Journal of Hydraulic Engineering* 116(5), 1990.

Kadlec, R.H. 1994. Detention and mixing in free water wetlands. *Ecological Engineering* 3, 345-380.

Kline, S. and F. McClintock. 1953. The description of uncertainties in a single-sample experiment. *Mechanical Engineering* January, 5-8.

Koch, E.W. 1993. Hydrodynamics of flow through seagrass canopies: Biological, physical and geochemical interactions. Ph.D. dissertation, Department of Marine Science, University of South Florida.

Kourta, A., H.C. Boisson, P. Chassaing and H.Ha Minh. 1987. Nonlinear interaction and the transition to turbulence in the wake of a circular cylinder. *Journal of Fluid Mechanics* 181, 141-161.

Kovasznay, L.S.G. 1948. Hot-wire investigation of the wake behind cylinders at low Reynolds numbers. *Proceedings of the Royal Society of London* 198A, 174-190.

Kundu, D., A. Haji-Sheikh, and D.Y.S. Lou. 1991. Heat transfer predictions in cross flow over cylinders between two parallel plates. *Numerical Heat Transfer, Part A* 19, 361-377.

Leonard, L.A., and M.E. Luther. 1995. Flow hydrodynamics in tidal marsh canopies. *Limnology and Oceanography* 40(8), 1474-1484.

Meroney, R.N. 1968. Characteristics of wind and turbulence in and above model forests. *Journal of Applied Meteorology* 7, 780-788.

Mugnier, Christophe G. 1995. Experimental study of the influence of vegetation on longitudinal dispersion. Master's Thesis, Department of Civil and Environmental Engineering, Massachusetts Institute of Technology.

Nierenberg, R.D. 1993. Detailed measurements on the effects of trees on wind speed, energy, vertical shear and turbulence. *Windpower '93,* American Wind Energy Association, 218-225.

Plate, E.J., and A.A. Quraishi. 1965. Modeling of velocity distributions inside and above tall crops. *Journal of Applied Meteorology* 4, 400-408.

Raupach, M.R., and A.S. Thom. 1981. Turbulence in and above plant canopies. *Annual Review of Fluid Mechanics* 13, 97-129.

Seginer, I., P.J. Mulhearn, E.F. Bradley, and J.J. Finnigan. 1976. Turbulent flow in a model plant canopy. *Boundary-Layer Meteorology* 10, 423-453.

Walker, G. 1982. Industrial heat exchangers: a basic guide. McGraw-Hill, New York.

Wang, F.C., T. Lu, and W.B. Sikora. 1993. Intertidal marsh suspended sediment transport processes, Terrebonne Bay, Louisiana, U.S.A. *Journal of Coastal Research* 9(1), 209-220.

Zavistoski, R.A. 1994. Hydrodynamics effects of surface piercing plants. Master's Thesis, Department of Civil and Environmental Engineering, Massachusetts Institute of Technology.

Zukauskas, A., and J. Ziugzda. 1985. Heat transfer of a cylinder in crossflow. Hemisphere Publishing Corporation, New York.

Appendix 1: Data curve modifications

smooth.m

```
function smooth=f(C)

Cm=zeros(1,length(C)-15);
for i=1:(length(C)-15)
        for j=0:15
                Cm(i)=Cm(i)+C(i+j);  [Cm is the sum of 16 consecutive data
        end                          points]
end
smooth=Cm/(16);                      [smooth is the smoothed curve, made up of the
plot(smooth);                        averages of all 16-point groups]
```

normal.m

```
function normal = f(C,x)             [C is smoothed concentration, x is a point beyond
                                     which concentration is essentially zero (determined
temp=C(x:length(C));                 visually from plotting the curve)]
Cmin=sum(temp)/length(temp);         [This finds the average pixel intensity at which dye
C=C-Cmin;                            concentration is zero & subtracts that out,
                                     essentially eliminating ambient light]
Cmax=max(C);                         [Maximum is taken directly from the curve]
normal=C/Cmax;
```

Appendix 2: Model of rate of increase of δ^* relative to δ

wakefr.m [Determines wake area fraction by modeling wakes in grid form]

```
wakeratio=[10 20 30 40 50];                    [Ratio of wake region to dowel size]
P=[0 0.005 0.006 0.01 0.014 0.015 0.02 0.025 0.03 0.035 0.04 0.045 0.05 0.053 0.055];
                                               [Dowel densities, area percentage]
for z=1:length(wakeratio);
        M=wakeratio(z);                        [Wake ratio for this iteration]
        for k=1:length(P)
                pop=P(k);                      [population for this iteration]
                nd=pop*1000;                   [Number of dowels in 1000 points]
                for j=1:100
                        A=0*(1:1000);
                        for i=1:nd;
                                n=floor(1000*rand);  [randomly spaces dowels]
                                nn=(n-M/2):(n+M/2); [creates wake of size (M+1)*dowel
                                                     (that is, includes dowel in wake)]
                                a=find(nn>0 & nn<1001);   [finds how much of wakes is
                                                           in area being looked at]
                                A(nn(a))=a./a;       [marks each point within a dowel/
                                                     wake region]
                        end;
                        wakefraction(j)=sum(A)/1000;[fraction of area taken up by wakes]
                end;
                MWF(z,k)=mean(wakefraction);   [finds mean fraction taken up by
                                               wakes over 100 trials]
        end;
end;

plot(P,MWF);
xlabel('dowel population - area fraction')
ylabel('wake area fraction')
```

59